

MEASUREMENT OF THE INCLUSIVE JET AND DIJET CROSS SECTIONS
USING 2010 DATA FROM THE ATLAS DETECTOR AND CALIBRATION
STUDIES AND SIMULATION OF THE ATLAS FORWARD CALORIMETER

by

Peter Thompson

A thesis submitted in conformity with the requirements
for the degree of Doctor of Philosophy
Graduate Department of Physics
University of Toronto

Copyright © 2011 by Peter Thompson

Abstract

Measurement of the inclusive jet and dijet cross sections using 2010 data from the ATLAS detector and calibration studies and simulation of the ATLAS forward calorimeter

Peter Thompson

Doctor of Philosophy

Graduate Department of Physics

University of Toronto

2011

(At most 150 words for M.Sc. or 350 words for Ph.D.)

Contents

1	The Standard Model	1
1.1	Overview	1
1.2	Quantum ChromoDynamics	4
1.2.1	Factorization	6
1.2.2	Perturbative QCD	9
1.2.3	Other Processes in Proton-Proton Collisions	11
1.2.4	Hadronization and Jet Production	11
1.2.5	MC event generators	12
2	Inclusive Jet and Dijet Cross Sections	15
2.1	Introduction	15
2.2	Overview of 2010 Running	17
2.3	Jets in ATLAS	18
2.3.1	Jet-Finding Algorithms	18
2.3.2	Jet Energy Scale Calibration	21
2.3.3	JES uncertainty	24
2.3.4	Jet Selection	26
2.4	Event Selection and Data Quality	29
2.4.1	Triggers used for the inclusive jet analysis	30
2.4.2	Transition Bin	34

2.4.3	Dijet Triggers	36
2.5	Unfolding	37
2.5.1	IDS method	39
2.5.2	Matching Efficiency	40
2.6	Treatment of uncertainties	42
2.6.1	Statistical uncertainties	42
2.6.2	Systematic Uncertainties	42
2.7	Results and discussion	44
2.7.1	Inclusive Jet Cross Section	44
2.7.2	Dijet Mass Spectrum	51
2.8	Summary	51
	Bibliography	60

Chapter 1

The Standard Model

1.1 Overview

The Standard Model (SM) describes the particles present in nature and the interactions between them. It has existed in its current form since 1978, and has been validated by numerous experiments since then [1, 2, 3]. All of the particles described in the Standard Model have been observed experimentally. Most recently, the observation of a particle “consistent” with the Higgs boson was announced on July 4th of 2012 [4, 5]. The cross sections and expected rates of production at the LHC’s design specifications are shown for several standard model particles in figure 1.1.

Elementary fermions in the Standard Model are divided into two groups: the quarks and leptons. These particles represent the fundamental building blocks of matter, and there are six “flavours” of each. For the quarks these are the up (u), down (d), charm (c), strange (s), top (t), and bottom (b). These may be organized into generations of mass, as follows,

$$\begin{pmatrix} u \\ d \end{pmatrix} \quad \begin{pmatrix} c \\ s \end{pmatrix} \quad \begin{pmatrix} t \\ b \end{pmatrix}, \tag{1.1}$$

where the upper members of each generation have electric charge $+2e/3$ and the lower

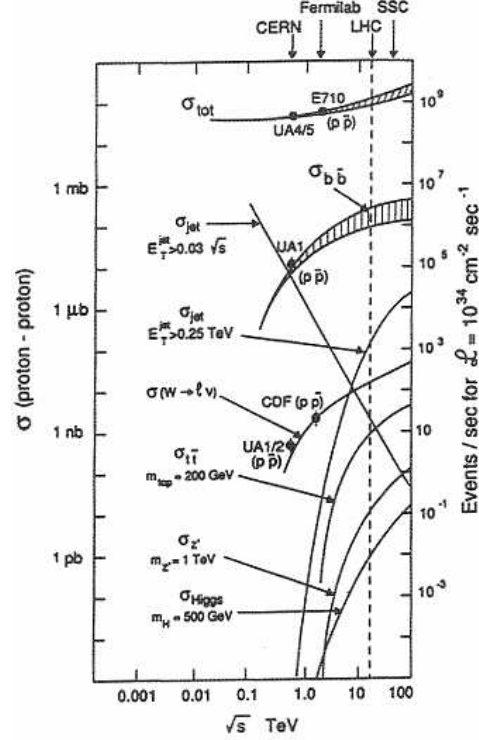


Figure 1.1: Production cross section for several SM particles as a function of the centre of mass energy of the pp collision. The dashed line corresponds to the design energy of the LHC, while the production rates on the right are obtained using the LHC's design luminosity.

members have charge $-e/3$. The leptons may be arranged in the same way, giving

$$\begin{pmatrix} \nu_e \\ e \end{pmatrix} \quad \begin{pmatrix} \nu_\mu \\ \mu \end{pmatrix} \quad \begin{pmatrix} \nu_\tau \\ \tau \end{pmatrix}, \quad (1.2)$$

where the lower members are the electron, muon, and tau, respectively, each having electric charge $-1e$. Each of these is paired with a neutrino (ν_x), which is neutral and (almost) massless. All quarks and leptons have a spin of $1/2$.

The strong, weak, and electromagnetic forces are also described by the Standard Model¹. These are described by gauge theories, such that the SM Lagrangian exhibits $SU(3)_c \otimes SU(2)_L \otimes U(1)_Y$ symmetry. The doublets listed in equations 1.1 and 1.2 reflect

¹gravity is not included in the SM, but its effects are negligible at the energy scales of interest.

the way in which the quark and lepton fields transform under the $SU(2)_L$ symmetry group, where the subscript L denotes that only the left handed components of the fields take part in this interaction. The $SU(2)_L$ and $U(1)_Y$ symmetries together describe the electroweak sector of the Standard Model, with the subscript Y referring to weak hypercharge² Quantum Chromodynamics (QCD) is the gauge theory that describes the strong (or colour) force and $SU(3)_c$ is the symmetry group associated with it, where the subscript C refers to colour charge.

Interactions between particles may occur via the weak force and the electromagnetic force. Quarks may also interact via the strong force, but leptons cannot. These interactions are mediated by gauge bosons, which are excitations of the gauge fields and act as force carriers. The strong force is carried by gluons, which are massless. There are eight types of gluon, corresponding to the 8 generators of the $SU(3)_c$ symmetry associated with the strong force. There would be four massless bosons arising from the $SU(2)_L \otimes U(1)_Y$ symmetries, however these symmetries are broken down to a single $U(1)_{EM}$ symmetry by the Higgs mechanism. This $U(1)_{EM}$ symmetry describes electromagnetic interactions, and the corresponding gauge boson is the massless photon. The other three gauge bosons associated with the broken symmetries are the W^+/W^- bosons which have a mass of 80.4 GeV, and the Z boson which has a mass of 91.2 GeV[6].

In addition to the gauge bosons, the Standard Model also contains a Higgs boson. The Higgs field allows the fermionic particles (and the gauge bosons of the weak force) to possess mass in a way that doesn't violate the gauge invariance of the SM Lagrangian. It is this mechanism that is responsible for the breaking of the electroweak ($SU(2)_L \otimes U(1)_Y$) symmetry. The Higgs field has a potential that makes it favorable for it to take a non zero vacuum expectation value. Fermions then interact with the Higgs field via a Yukawa coupling, and so when the Higgs field takes a vacuum expectation value these couplings

²The weak hypercharge of a particle is the sum of its electric charge and the third component of its weak isospin (T_3). Up-type quarks and neutrinos have $T_3 = 1/2$, while down-type quarks and charged leptons have $T_3 = -1/2$.

act as mass terms in the Lagrangian while retaining their gauge invariance.

1.2 Quantum ChromoDynamics

Quantum ChromoDynamics (QCD) is a non-Abelian gauge theory based on $SU(3)_c$. It is the strongest of the three interactions in the Standard Model, and affects quarks but not leptons. As the LHC collides beams of protons, QCD is the dominant interaction.

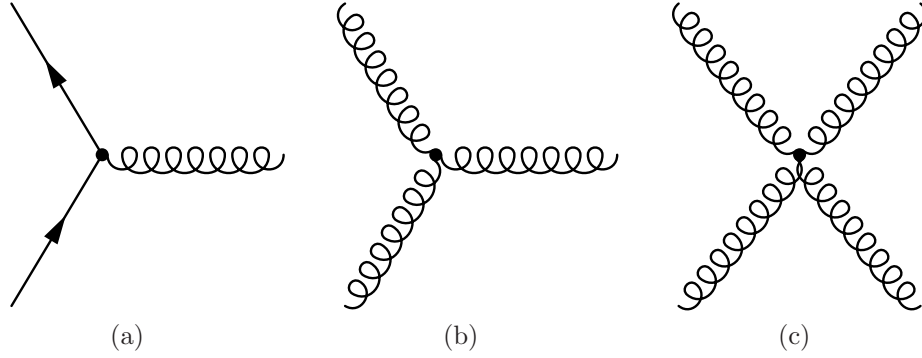


Figure 1.2: Feynman diagrams depicting the vertices of QCD.

Feynman diagrams for QCD vertices are shown in figure 1.4. A major difference of QCD compared to quantum electrodynamics (QED) is that gluons carry colour charge and thus interact with themselves, while the photon is chargeless. Gluon-gluon interactions can occur via the three gluon or four gluon vertices, which are depicted in figures 1.2(b) and 1.2(c).

The coupling constant, α_s , describes the strength of QCD interactions. This varies as a function of momentum, such that the strength of the coupling at two different momentum scales, p^2 and Q^2 , are related by

$$\alpha_s(p^2) = \frac{\alpha_s(Q^2)}{1 + \frac{11-(2/3)N_f}{4\pi}\alpha_s(Q^2)\log(\frac{p^2}{Q^2})} \quad (1.3)$$

where N_f is the number of quark flavours with mass less than p^2 . The “QCD scale”,

Λ_{QCD} , is defined as the scale at which the denominator of equation 1.3 vanishes, such that

$$\frac{11 - (2/3)N_f}{4\pi} \alpha_s(Q^2) \log\left(\frac{\Lambda_{QCD}^2}{Q^2}\right) = -1. \quad (1.4)$$

Using this definition, equation 1.3 becomes

$$\alpha_s = \frac{4\pi}{(11 - (2/3)N_f) \log\left(\frac{-p^2}{\Lambda_{QCD}^2}\right)}. \quad (1.5)$$

The value of Λ_{QCD} is around 200-300 MeV. This does not mean that the coupling constant is infinite at Λ_{QCD} , merely that the perturbative calculations used in the derivation of eqn 1.3 are no longer valid in this regime. When measured at the mass of the Z boson, the coupling constant $\alpha_s(M_Z) = 0.1184[6]$, indicating that perturbation theory is reliable at this energy scale.

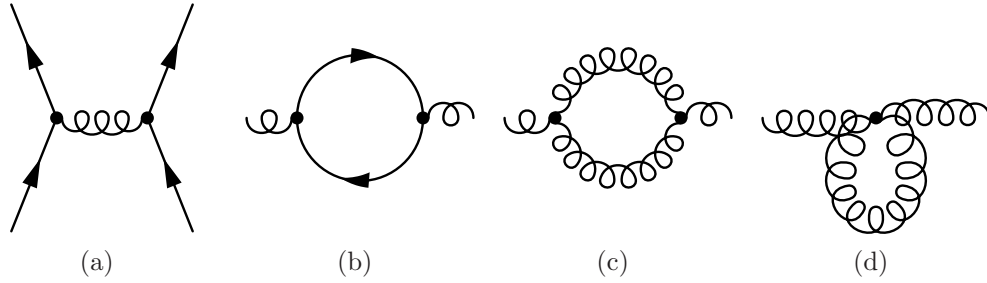


Figure 1.3: Tree level $qq \rightarrow qq$ scattering, and vacuum polarization diagrams.

A leading order diagram for a $qq \rightarrow qq$ process is shown in figure 1.3(a), where four-momentum is exchanged between two quarks via a gluon. At next to leading order (NLO), the gluon propagator in figure 1.3(a) may be replaced by the vacuum polarization diagrams shown in figures 1.3(b)-1.3(d). The first of these diagrams, figure 1.3(b), causes the vacuum to effectively screen colour charge, such that at large distances the strength of the interaction is diminished.

The three and four gluon vertices give rise to the diagrams in figures 1.3(c) and 1.3(d). The gluon loops in these diagrams cause an anti-screening effect, such that the

strength of the interaction decreases as the exchanged four-momentum increases. This is the opposite effect to that seen for the quark loop, however in QCD it is this effect that dominates.

The anti-screening effect is characteristic of $SU(N)$ gauge theories. An $SU(4)$ theory would contain four colours and 15 gluon fields ($N^2 - 1$), increasing the contribution of the gluon loop diagrams in figure 1.3 and thus increasing the anti-screening effect. Conversely, a QCD-like theory based on $SU(2)$ would contain 3 gluons (c.f. the three gauge bosons of the weak force), which would result in a smaller anti-screening effect. The screening effect, however, increases with the number of quark fields contained in the theory. For example, in $SU(3)$ gauge theories that contain 17 or more quark flavours the screening effect is dominant and the strength of the interaction increases as the exchanged four-momentum increases, as can be seen from equation 1.5.

1.2.1 Factorization

Theoretical calculations regarding proton-proton collisions are complicated, as different energy scales are involved in the problem. The four-momentum exchanged between partons is at the TeV scale for collisions at the LHC, while the physics describing the arrangement of the partons within the proton is determined at a much lower scale, Λ_{QCD} . QCD is a strongly coupled theory at low energies, whereas at higher scales it is weakly coupled and perturbative methods may be used. Fortunately, factorization allows the physics at these different scales to be separated [7]. The low momentum, non-perturbative physics describing the structure of the proton may be isolated from the high momentum, parton-parton scattering.

The structure of the proton may thus be described using Parton Distribution Functions (PDFs), $q_i(x, Q^2)$, $G(x, Q^2)$, and $\bar{q}_i(x, Q^2)$. The functions $q_i(x, Q^2)$ describe the probability of a probe (such as an electron or parton) with momentum Q^2 resolving a quark of flavour i within the proton, with said quark carrying a fraction x of the proton's

momentum[8]. Similarly, the distribution functions $\bar{q}_i(x, Q^2)$ and $G(x, Q^2)$ describe the probability of resolving an antiquark or gluon, respectively, within the proton. While a proton is typically thought of as containing two up quarks and one down quark, it also contains a number of gluons, which carry about half of the proton's momentum. Gluons may also split into quark-antiquark pairs, referred to as “sea” quarks. Because of this, the probabilities of finding antiquarks (or quarks with flavours other than up or down) are non-zero, and vary as a function of Q^2 [9]. The number of valence quarks is conserved, however, giving the conditions

$$\int_0^1 dx [q_{\text{up}}(x, Q^2) - \bar{q}_{\text{up}}(x, Q^2)] = 2 \quad (1.6)$$

$$\int_0^1 dx [q_{\text{down}}(x, Q^2) - \bar{q}_{\text{down}}(x, Q^2)] = 1 \quad (1.7)$$

$$\int_0^1 dx [q_j(x, Q^2) - \bar{q}_j(x, Q^2)] = 0 \quad , \quad j \in \{c, s, t, b\} \quad (1.8)$$

While the parton distribution functions must be determined from experiment, their Q^2 dependence can be calculated in a similar fashion to that of the coupling constant, α_s . The dependence of the PDFs on Q^2 is given by the Dokshitzer - Gribov - Lipatov - Altarelli - Parisi (DGLAP) equations [10, 8]:

$$\frac{dq_i(x, Q^2)}{d \log Q^2} = \frac{\alpha_s}{2\pi} \int_x^1 \frac{dy}{y} \left[P_{qq}(y) q_i\left(\frac{x}{y}, Q^2\right) + P_{qG}(y) G\left(\frac{x}{y}, Q^2\right) \right] \quad (1.9)$$

$$\frac{d\bar{q}_i(x, Q^2)}{d \log Q^2} = \frac{\alpha_s}{2\pi} \int_x^1 \frac{dy}{y} \left[P_{qq}(y) \bar{q}_i\left(\frac{x}{y}, Q^2\right) + P_{qG}(y) G\left(\frac{x}{y}, Q^2\right) \right] \quad (1.10)$$

$$\begin{aligned} \frac{dG(x, Q^2)}{d \log Q^2} = & \frac{\alpha_s}{2\pi} \int_x^1 \frac{dy}{y} \left[P_{Gq}(y) \sum_i \left(q_i\left(\frac{z}{y}, Q^2\right) + \bar{q}_i\left(\frac{x}{y}, Q^2\right) \right) \right. \\ & \left. + P_{GG}(y) G\left(\frac{x}{y}, Q^2\right) \right], \end{aligned} \quad (1.11)$$

where the P_{xx} are splitting functions. While a probe at Q^2 may resolve (i.e. “see”) a quark or gluon within the proton, a probe with higher momentum may be able to resolve

finer structures that are only present for a short time. For example, a given probe may be able to resolve a quark, while a probe with higher momentum may be able to interact with a collinear gluon emitted by this quark (fig 1.4(a)). Similarly, a high momentum probe may be able to resolve a quark or antiquark produced by a gluon (fig 1.4(b)). The splitting function $P_{Gq}(y)$ describes the probability that a gluon will be resolved within a quark, carrying a fraction y of the quark momentum. The complementary function $P_{qq}(y)$ describes the probability that a quark will still be resolved as a quark at higher momenta, while the functions $P_{qG}(y)$ and $P_{GG}(y)$ describe the probability of resolving quarks and gluons, respectively, from a gluon.

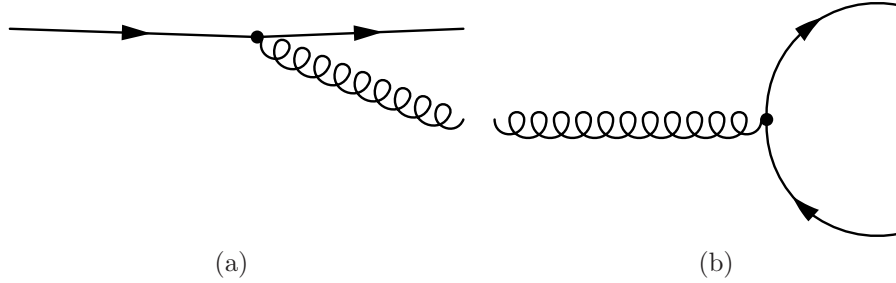


Figure 1.4: Processes described by the splitting functions. In figure 1.4(a), a quark emits a collinear gluon. A high momentum probe may be able to resolve the emitted gluon.

The PDFs derived by the CT10 group [11] are plotted in figure 1.5. These are derived from fixed target deep inelastic scattering results carried out at HERA [12], as well as data obtained from proton-proton collisions at the Tevatron [13]. At small x the gluon PDF is dominant, and consequently the sea quark contributions are also significant in this regime, whereas the valence quarks dominate at higher values of x .

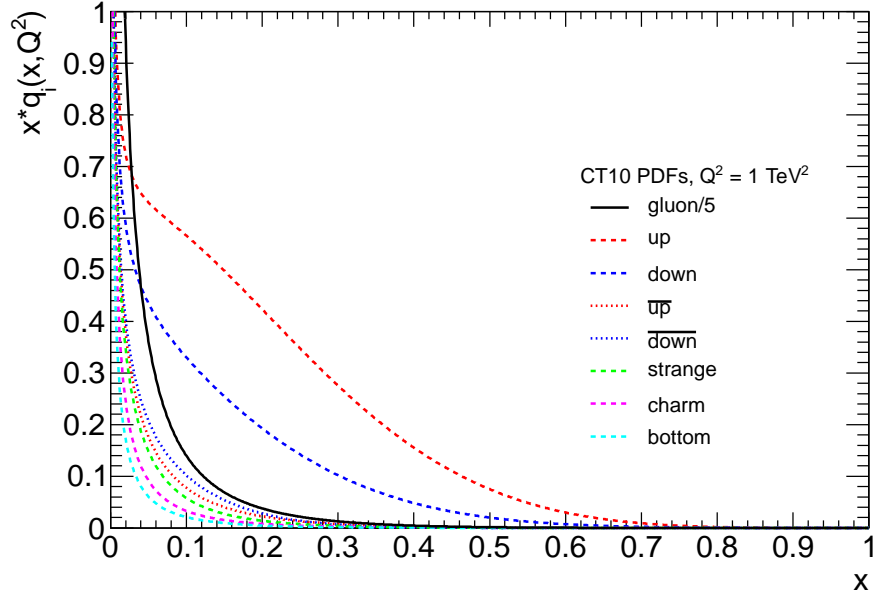


Figure 1.5: CT10 pdfs, obtained at a momentum scale of 1 TeV [14, 11]. Note that the y axis shows the product of the pdf and x . The area under a given curve thus corresponds to the relative amount of the proton's momentum carried that type of parton.

1.2.2 Perturbative QCD

The cross section for producing a final state, X , from two protons with four-momentum p_A and p_B may be written as [15]

$$\sigma_{pp \rightarrow X} = \sum_{i,j} \int_0^1 dx_1 \int_0^1 dx_2 f_{i,A}(x_1, Q^2) f_{j,B}(x_2, Q^2) \hat{\sigma}_{i,j \rightarrow X}(x_1 p_A, x_2 p_B), \quad (1.12)$$

where $f_{i,A}$ is the parton distribution function describing the probability of finding a parton of flavour i within proton A , and the sum runs over all parton flavours (i.e. quark and gluon flavours). The cross section, $\hat{\sigma}_{i,j \rightarrow X}$, describes the probability of producing the final state X from the incoming partons of flavour i and j , and may be calculated order by order in perturbation theory.

A leading order diagram for a $2 \rightarrow 2$ process is shown in figure 1.6(a). Leading order contributions are the easiest to calculate, but are generally only correct to within an order

of magnitude [16]. Theoretical predictions that are to be compared with experimental measurements usually need to be made at next to leading order (NLO) or higher.

At NLO, virtual corrections arising from loop diagrams (such as the one shown in figure 1.6(b)) must be considered. These virtual corrections contain ultraviolet divergences, which may be removed through renormalization. However, there are also infrared divergences present, such that the result diverges in cases where the energy of an incoming or outgoing parton vanishes (“soft” divergence), or in cases where the separation between two of the initial or final state partons vanishes (a “collinear” divergence). These infrared divergences cannot be removed, and so any calculation carried out to a fixed order in perturbation theory that considers a specific number of partons in the final state will diverge [17]. In order to obtain a physical result at fixed order in perturbation theory, real corrections must be considered. These real corrections include cases where an additional parton is emitted by one of the incoming or outgoing partons, such as that shown in figure 1.6(c). The real corrections also include collinear and soft divergences, but of the opposite sign to those present in the virtual corrections. In fixed order calculations in which both real and virtual contributions are considered, the infrared divergences cancel to give a finite result[16].

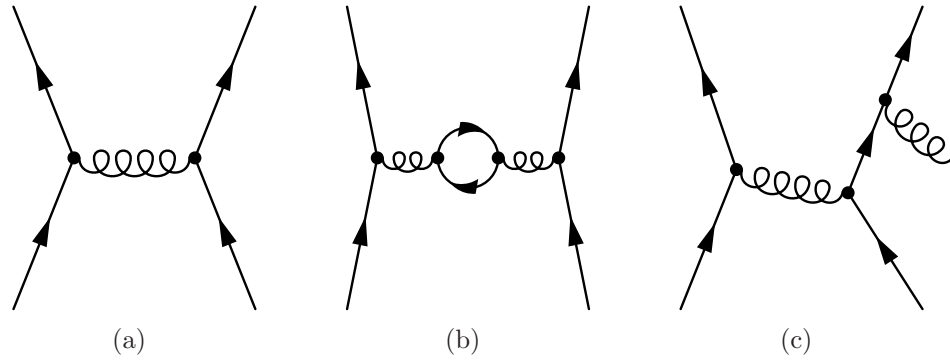


Figure 1.6: Diagrams for $qq \rightarrow qq$ scattering. The tree diagram in (a) contributes at leading order, while the virtual correction in (b) and the real correction in (c) contribute at NLO.

1.2.3 Other Processes in Proton-Proton Collisions

The products of hard scatterings between partons are usually considered the most interesting parts of proton proton collisions. However, there are other important processes involved in these collisions. Partons entering or leaving the hard scattering may undergo bremsstrahlung emission, producing initial (or final) state radiation.

There are also underlying event effects associated with the proton remnants, i.e. other partons that were members of the initial protons but were not involved in the hard scattering. These partons may undergo soft scatterings amongst themselves (multiple parton interactions), and may also radiate before/after these interactions.

“Pile-up” is another issue affecting the LHC³. The LHC collides bunches containing $\sim 10^{11}$ protons. It is rare for only a single scattering to occur during bunch crossings. At the LHC’s design specifications, there will be ~ 23 collisions every bunch crossing. The majority of these collisions are soft, producing low p_T products. However, the energy deposited in the calorimeter by pile-up needs to be accounted for when measuring other high p_T objects.

1.2.4 Hadronization and Jet Production

After the hard scattering and emission of any final state radiation, partons will continue to interact via the colour force. As the separation between these partons increases, the strength of the interaction also increases.

The confinement hypothesis states that colour charged partons do not exist in isolation, they must be confined within colourless hadrons[8]. All hadrons observed in nature consist of quarks and gluons arranged in colour singlet (i.e. colour neutral) states. If a given quark were to be separated from the other constituents in its parent hadron in order to “isolate” it, the energy required to achieve this would increase with the separation

³While pileup is a significant problem at the LHC’s design luminosity (and at present), it was not a major issue during 2010.

distance. At a certain point it becomes energetically favourable for a quark-antiquark pair to be produced from the vacuum, such that the remnants of the parent hadron form a bound state with one member of the new pair, while the separated quark binds with the other member of the pair. It is thus not possible to observe a free quark in isolation, as new hadrons are formed instead using partons created from the vacuum.

Partons emerging from the collision thus organize themselves into collimated sprays of hadrons, which are referred to as “jets”. The showering and hadronization of particles are non-perturbative processes, and so it is difficult to predict the way in which a parton produced in a collision will evolve into a jet. The experimental measurement of the inclusive jet cross section obtained using 2010 data is discussed in chapter 2, while the algorithms used to define jets are described in section 2.3.1.

1.2.5 MC event generators

Event generators are Monte Carlo programs that simulate high energy physics events, and thus may be used to obtain theoretical predictions for the results of a given analysis. In the context of ATLAS, these programs are used to simulate proton-proton collisions, incorporating initial state radiation, final state radiation, and underlying event effects. The output of an event generator consists of a list of stable particles, which may then be passed to a detector simulation program such as `GEANT4` (discussed in section ??). The results of the detector simulation may then be analysed in the same manner as real data, allowing theoretical and experimental results to be compared.

Parton Shower Monte Carlo programs, such as `PYTHIA` [18] and `HERWIG` [19], factorize the collision into different stages. These consist of the hard scattering between partons, and initial (final) state radiation emitted by incoming (outgoing) partons, as illustrated in figure 1.7. The hard scattering is determined first, using the leading order cross section for the hard process. As the hard process involves a large four momentum transfer, the incoming and outgoing partons will have high values of p^2 and thus be off the mass

shell. The incoming and outgoing partons are then “showered” in order to produce the initial/final state radiation. Outgoing partons undergo a series of time-like emissions in which additional partons are radiated. These emissions reduce the q^2 of the involved partons, as the final state partons must be on the mass shell. The probability that an emission will occur is given by the relevant splitting function, P_{xx} , (introduced in the DGLAP equations 1.11) multiplied by a Sudakov form factor. The Sudakov factor is essentially a resummation of virtual corrections at leading logarithmic (LL) level [20, 21] and conserves probability such that the chance for a series of emissions to occur never exceeds unity.

Initial state radiation is treated similarly to final state radiation, but in reverse. As the hard scattering is computed first, the properties of the partons just prior to the scattering have already been determined. These incoming partons are then evolved backwards in time, undergoing repeated emission until they become on-shell constituents of the colliding protons.

Parton shower Monte Carlo generators typically include methods to model multiple parton interactions in order to describe the underlying event. For events generated by HERWIG, this is handled by the JIMMY library [22]. These models depend on a number of parameters (such as a minimum p_T threshold for scattered partons). The values of these parameters define a specific “tune” of the generator. The ATLAS Minimum Bias Tune (AMBT2B) and ATLAS Underlying Event Tunes (AUET2B) [23] are used in some of the theoretical predictions presented in section 2.7.1, as is the Perugia2011 tune [24].

While parton shower MC generators calculate the hard scattering process at LO, matrix element generators such as POWHEG [25] and NLOjet++ [26] treat the hard scattering at NLO in perturbative QCD. These generators use a subtraction [16] technique, in which a term is subtracted from the real corrections and added to the virtual corrections such that both sets of corrections may be evaluated numerically. This allows the cross section for the hard scattering to be calculated at full NLO accuracy.

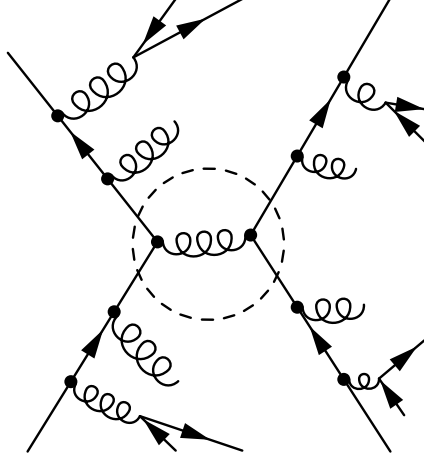


Figure 1.7: In shower Monte Carlo programs, the hard scattering (inside the dashed circle) is computed first at leading order. The partons entering (exiting) this scattering are then showered to produce the initial (final) state radiation.

Parton shower MC generators are good at handling soft emissions, whereas matrix element generators are accurate to NLO and are capable of generating events containing multiple well-separated jets. Matrix element generators may be used to compute the hard scattering before passing the incoming and outgoing partons to shower MCs to model the soft emissions. However, this has to be done carefully, as some contributions at NLO are included within the LL resummation used by the shower MCs, and so simply showering the output from an NLO ME would double count these contributions. Recently the POWHEG box [27] formalism has been applied to dijets [28], which allows the shower MCs to appropriately interface with the ME calculation. The contribution from the shower MC is subtracted during the ME calculation, so that the calculation is done consistently. POWHEG is used in this fashion for some of the theoretical predictions presented in section 2.7.1.

Chapter 2

Inclusive Jet and Dijet Cross Sections

2.1 Introduction

The inclusive jet cross section refers to the cross section for jet production with no discrimination based on the final state, i.e. all jets in each event are considered. The cross section measurement is binned in terms of the transverse momentum, p_T , and the jet rapidity, y .

The first ATLAS measurement of the inclusive jet and dijet cross sections was made in 2010 [29, 30], using 17nb^{-1} of early data collected from 7 TeV collisions. The jet production cross section was measured for jets with p_T from 60 to 600 GeV and with rapidities less than 2.8 in magnitude. This measurement was updated in early 2011 using the full 2010 ATLAS dataset (37pb^{-1}) to extend those results. This update expanded the kinematic coverage of the measurement to include jets with p_T from 20 GeV to 1.2 TeV, and the rapidity range was extended into the forward region to include jets with $|y| < 4.4$. Figure 2.1 shows the kinematic region covered by the initial measurement compared to that described in this analysis. The dijet mass spectrum has also been

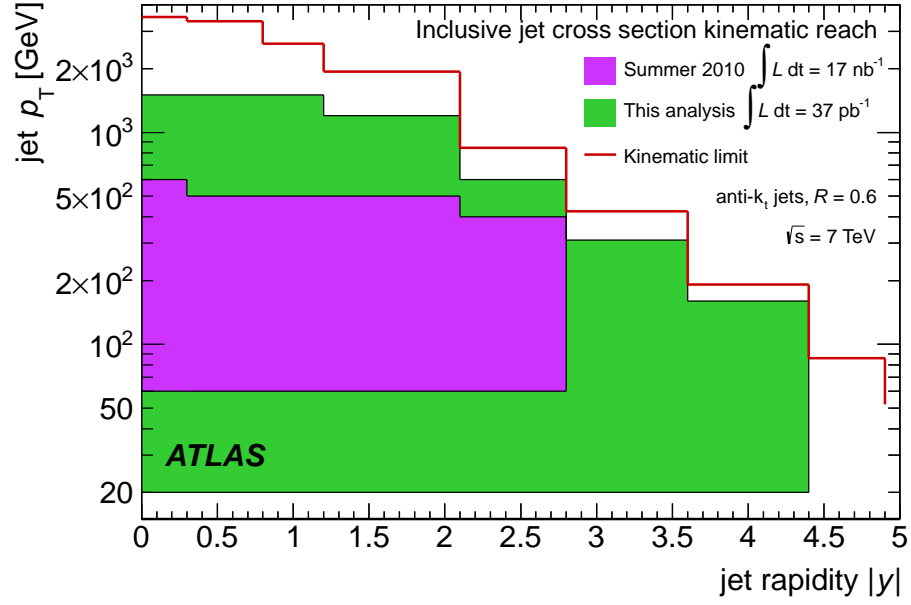


Figure 2.1: Diagram showing the kinematic range covered by the first inclusive jet cross section measurement using 17nb^{-1} (purple) of early data, and that covered when using the full 37pb^{-1} from the 2010 dataset (green).

measured using 2010 data, and the rapidity coverage of this measurement has also been expanded to include the forward region. The results discussed here have been presented as a conference note [31] and were published in 2012 [32]. The inclusive jet cross section has also been measured using the CMS detector [33, 34], however these measurements treat the regions $|y| < 3$ and $3.2 < |\eta| < 4.7$ separately. The ATLAS measurement discussed in this chapter has no gaps in the rapidity coverage.

Section 2.2 gives a brief overview of the operation of ATLAS and the LHC during 2010, while Section 2.3 describes how jets are defined and calibrated in ATLAS data. The event selection and triggers used for data collection are described in section 2.4, while section 2.5 describes the method used to correct for detector resolution effects in the measured data (“unfolding”). The treatment of experimental uncertainties is described in section 2.6, and results are presented in section 2.7.

2.2 Overview of 2010 Running

Data taken during 2010 has been divided into nine data periods, A-I. Each period represents an interval during which there were no major changes to the configuration of the detector and trigger. Each run is subdivided into a number of luminosity blocks (LB), each of which corresponds to ~ 2 minutes worth of recorded data. The instantaneous luminosity achieved by the LHC improved over the course of the year as the accelerator was commissioned, from $2 \times 10^{27} \text{cm}^{-2} \text{s}^{-1}$ early in the year to $2 \times 10^{31} \text{cm}^{-2} \text{s}^{-1}$ by the end of pp running. At present (Fall 2012), the LHC is running with an instantaneous luminosity is around $7 \times 10^{33} \text{cm}^{-2} \text{s}^{-1}$, which slightly less than the design luminosity of $10^{34} \text{cm}^{-2} \text{s}^{-1}$.

The amount of data delivered by the LHC and recorded at ATLAS throughout 2010 is shown in figure 2.2. In total ATLAS recorded 45 (nb)^{-1} of data from pp collisions. Note that this value is slightly lower than the integrated luminosity delivered by the LHC (48.1 (nb)^{-1}). The Inner Detector contains sensitive electronics, and so is only supplied with high voltage after stable running conditions have been established. This is the main reason for the discrepancy between the amount of data delivered and that recorded.

Certain data quality (DQ) requirements were made to ensure that the data used in this analysis was recorded when all relevant systems were functioning correctly. Specifically, it was required that the calorimeters, inner detector (pixel, SCT and TRT), luminosity detectors and trigger systems (L1 CTP, L1 Calo, and the HLT when applicable) were functioning normally, and also that performance criteria were met when reconstructing jets, missing energy and tracks. After imposing these conditions, the analysis is carried out using the remaining 37 (nb)^{-1} of data.

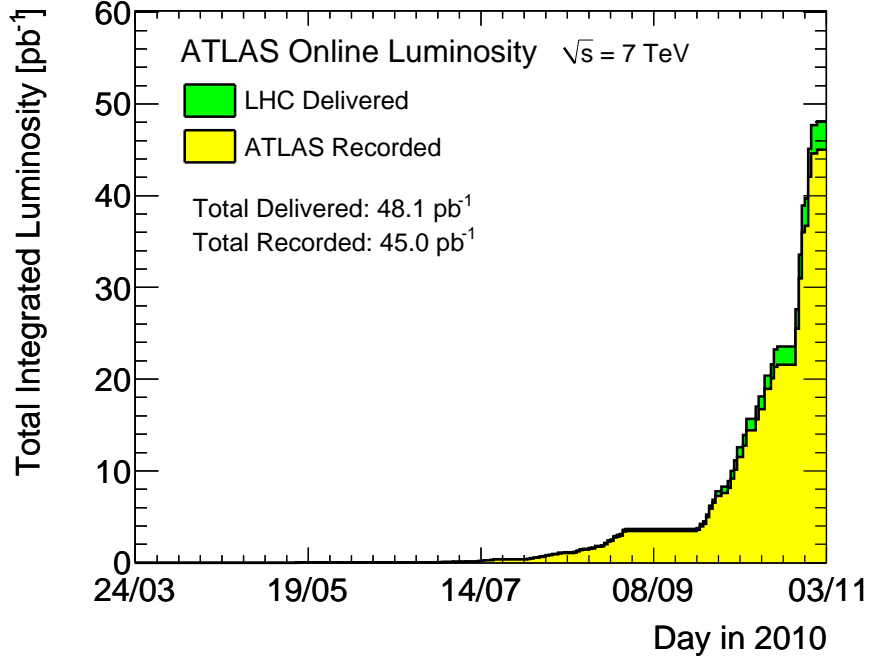


Figure 2.2: Integrated luminosity recorded by ATLAS over the course of 2010.

2.3 Jets in ATLAS

For the inclusive jet cross section and dijet analyses, jets were reconstructed using the anti- k_t algorithm running on topologically clustered calorimeter cells. In this section jet finding algorithms will be presented, followed by a discussion of the jet calibration method and the uncertainty on the jet energy scale.

2.3.1 Jet-Finding Algorithms

Jet finding algorithms are run on a set of input objects, which are referred to as constituents. In general any object with an associated four vector may be used as a constituent, however for this analysis topoclusters (discussed in section ??) are the only constituents considered.

The jets considered in this analysis are reconstructed using the anti- k_t algorithm [35]. The family of k_t -like jet algorithms operate by forming a list of all the constituents in

the event. For all constituents and pairs of constituents, the jet resolution quantities

$$d_{ij} = \min(k_{ti}^{2p}, k_{tj}^{2p}) \frac{(y_i - y_j)^2 + (\phi_i - \phi_j)^2}{R^2} \quad (2.1)$$

and

$$d_i = k_{ti}^{2p} \quad (2.2)$$

are computed, where k_{ti} , ϕ_i and y_i are the transverse momentum, azimuthal angle and rapidity of the i -th constituent, respectively. The distance parameter R is related to the desired size of the jets being found, such that the reconstructed jets will be separated by no less than R in (y, ϕ) -space. The parameter p defines the jet-finding algorithm: $p = 1$ corresponds to the k_t algorithm [36], $p = -1$ gives the anti- k_t algorithm, and $p = 0$ corresponds to the Cambridge-Aachen cone algorithm [37].

Once the d_{ij} and d_i have been computed, the values are sorted. If the smallest value present corresponds to a d_{ij} , then the i -th and j -th constituents are formed into a proto-jet by summing their four momenta. The proto-jet is then added to the list of constituents and its components are removed. The d_{ij} and d_i values are then recomputed for all remaining constituents and proto-jets. This process is repeated, with each iteration either adding constituents to an existing proto-jet or merging constituents to form a new one. In the case where a d_i value is smaller than any d_{ij} value, then this proto-jet is taken as a complete, final jet and is removed from the list. The process continues until the constituent list is empty, with all constituents having been used to form complete jets. The the four momentum of a jet is obtained by summing the four momenta of its constituents. A jet mass may then be defined by calculating the invariant mass of the jet's four momentum.

In the k_t algorithm, d_{ij} is approximately equal to the relative difference in transverse momentum between the two constituents i and j , in the limit where the angle between them is small. The k_t algorithm thus clusters together constituents with similar momenta.

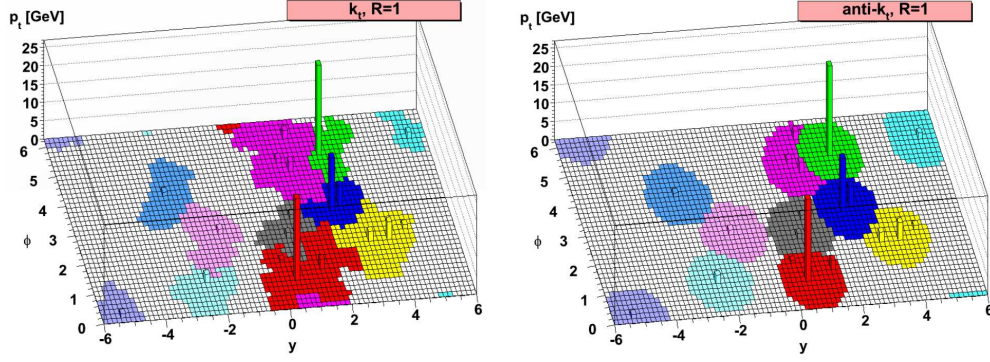


Figure 2.3: jets found by the k_t algorithm (left) and the anti- k_t algorithm (right). The event was generated using HERWIG [?], and contains some soft radiation in addition to the high- p_T constituents[35].

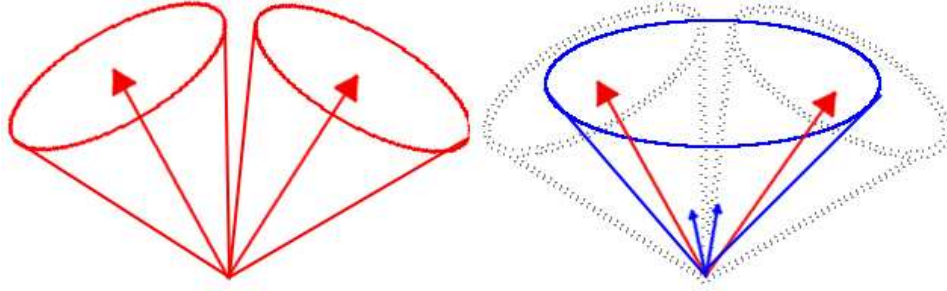


Figure 2.4: Illustration of a jet algorithm which is not IR safe. In the figure on the left, two distinct jets are found around the high-pt constituents. In the presence of soft radiation (right), The algorithm finds only a single jet.

As showering partons tend to radiate collinearly, the k_t algorithm thus acts to collect all of these radiated constituents and recombine them into a single jet.

However, this procedure clusters constituents with the smallest transverse momenta first, such that high p_T constituents may be clustered around groups of low p_T constituents. This results in jets with irregularly shaped boundaries, as shown in Figure 2.3(a). Conversely, the anti- k_t algorithm considers the highest p_T constituents first and builds the proto-jets around those, resulting in conically-shaped jets (as shown in Figure 2.3(b)). This also means that jets found by the anti- k_t algorithm tend to be less sensitive to the effects of pile-up and the underlying event [35].

The k_t -like jet algorithms are favored because they are both infrared (IR) and collinear

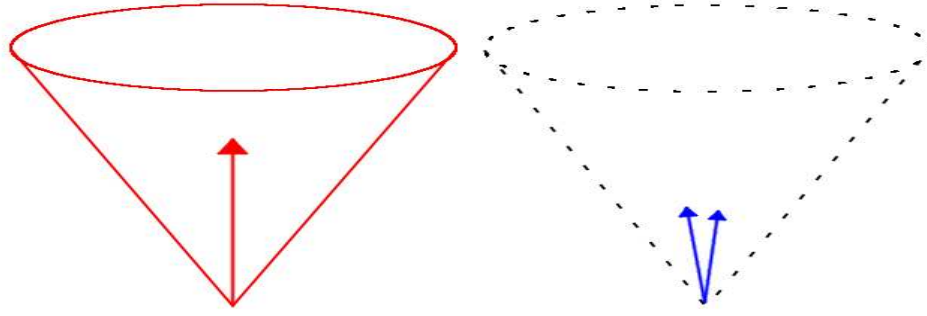


Figure 2.5: Illustration of an algorithm which is not collinear safe. On the left, a jet is found around a single high-pt constituent. On the right, the single constituent is replaced by two constituents, each with half the p_T of the original. In this case, the algorithm fails to find a jet.

safe. IR safety means that the jets found are stable with respect to the presence of low p_T constituents arising from pile-up or the underlying event. For an algorithm to be IR safe, the presence of soft particles can not “confuse” the algorithm into mistaking two separate jets for a single large jet, as illustrated in Figure 2.4. Collinear safety requires that the algorithm will still find a jet if, for instance, a single high- p_T constituent is replaced by two (or more) close together constituents with lower p_T (fig 2.5). The k_t -like algorithms have these properties, whereas most iterative cone algorithms tend not to.

2.3.2 Jet Energy Scale Calibration

Once a jet has been defined, its energy must be calibrated to the Jet Energy Scale (JES). This is done through an “EM+JES” scheme, whereby the EM scale energy of the jet is multiplied by a calibration factor to obtain the energy at the JES. The calibration is derived from Monte Carlo simulations using a numerical inversion process.

The calibration is done in three steps. First, the EM scale energy of the jet is adjusted in order to correct for pile-up effects. Additional proton-proton interactions from the same event can deposit energy in the calorimeter, affecting the energy of the high p_T objects from the hard scattering. Minimum bias data are used to determine the aver-

age energy deposited in the calorimeter as a function of pseudorapidity and the number of primary vertices reconstructed from the event. This information is used to subtract the average EM scale energy added to the jet as a result of pileup.

The second step is to correct the kinematics of the jet, still at the EM scale, based on the location of the hard scattering. Initially, jet kinematics are computed using the geometrical centre of **ATLAS** as the origin of the jet. The luminous region of **ATLAS** has a width of $\sim 40 - 70 \mu\text{m}$ in the transverse directions and $\sim 22 \text{ mm}$ longitudinally [38], and it is within this volume that the hard scatterings occur. The vertex with the highest sum of squared transverse momenta from tracks ($\sum p_{T,track}^2$) is taken as the position of the hard scatter, and all jet kinematic quantities (p_T, y, ϕ , etc) are recomputed using this vertex as the origin.

Finally, the JES correction is applied. The correction is derived exclusively from Monte Carlo, using samples generated without the inclusion of pile-up. An event generator is used to simulate a hard parton-parton scattering typical of proton-proton collisions, which outputs a set of final state particles and their four momenta. **GEANT4** is then used to simulate the interaction of these particles with the detector. The event is then reconstructed using the same methods that are used for the data: calorimeter cells are reconstructed and used to form topological clusters, on which jet finding algorithms are run. “Truth” jets are formed by running the jet finding algorithms on the final state particles output by the event generator.

The JES calibration accounts for the following effects:

- non-compensation of the calorimeter, i.e. the energy is calibrated to the hadronic scale;
- energy deposited in inactive (uninstrumented) regions of the detector;
- leakage effects from particle showers not fully contained in the calorimeters;
- particles contained in the truth jet but not in the reconstructed jet;

- energy from showering particles that is not collected by the topoclustering algorithm (out of cluster corrections).

The calibration is derived by comparing the jets reconstructed from the (simulated) calorimeter information to the truth jets. A reconstructed jet is matched to a truth jet if the distance between them satisfies $\Delta R < 0.3$, where $\Delta R = (\Delta\eta^2 + \Delta\phi^2)^{1/2}$. Jets are only considered if they are isolated in order to avoid mis-matching in cases where multiple jets are close together. A reconstructed/truth jet must have no other jets with $p_{T,EM} > 7\text{GeV}$ within $2.5R$, or it is not used in the derivation of the calibration.

The matched reconstructed-truth jet pairs are then used to define the response R , such that

$$R = \frac{E_{\text{reco}}^{\text{EM}}}{E_{\text{truth}}}, \quad (2.3)$$

where $E_{\text{reco}}^{\text{EM}}$ is the EM scale energy of the reconstructed jet and E_{truth} is the energy of the truth jet. The response is binned in E_{truth} and η_{det} , the pseudorapidity of the reconstructed jet at the EM scale. For each $(E_{\text{truth}}, \eta_{\text{det}})$ bin, the mean reconstructed jet energy, $\langle E_{\text{reco}}^{\text{EM}} \rangle$, is found, and a Gaussian fit is used to extract the mean response, $\langle R \rangle$.

The response is then parameterized as a function of $E_{\text{reco}}^{\text{EM}}$ for each η_{det} bin. For the k -th η_{det} bin, a fit is performed on the $(\langle E_{\text{reco}}^{\text{EM}} \rangle, \langle R \rangle)$ points obtained from each E_{truth} bin. The fitted function is of the form

$$F_{\text{calib},k}(E_{\text{reco}}^{\text{EM}}) = \sum_{j=0}^{N_{\text{max}}} a_j (\log E_{\text{reco}}^{\text{EM}})^j, \quad (2.4)$$

where the a_j are free parameters and N_{max} is an integer between 1 and 6.

The correction factor is then found by inverting $F_{\text{calib},k}$, so the final EM+JES energy of a jet lying in the k -th η_{det} bin is given by

$$E_{\text{reco}}^{\text{JES}} = \frac{E_{\text{reco}}^{\text{EM}}}{F_{\text{calib},k}(E_{\text{reco}}^{\text{EM}})}. \quad (2.5)$$

2.3.3 JES uncertainty

The systematic uncertainty on the JES is an important quantity, and one of the dominant sources of uncertainty in the inclusive jet and dijet cross section analyses. There are several sources that contribute to this uncertainty, outlined below:

- Uncertainty from the calibration method** The EM+JES method calibrates jets by applying a correction factor to the EM scale energy of the jet. This treats all of the jets constituents equally, each constituent is effectively scaled by the same calibration factor. Additionally, this same correction factor is used for both the energy and transverse momenta of the jet, which may bias the calibrated p_T in cases where the calibrated jet mass differs from the mass of the truth jet. The uncertainty arising from the calibration method is estimated by comparing the reconstructed jets at the EM+JES scale to their truth jet counterparts. The responses $\langle R_E \rangle = \langle E_{\text{reco}}^{EM+JES} / E_{\text{truth}} \rangle$ and $\langle R_P \rangle = \langle p_{T,\text{reco}}^{EM+JES} / p_{T,\text{truth}} \rangle$ are computed, and binned in terms of $p_{T,\text{reco}}^{EM+JES}$. Any deviation of $\langle R_E \rangle$ or $\langle R_P \rangle$ from unity suggests that the kinematics of the reconstructed jets after calibration are not equal to those of the truth level jets (non-closure). The estimated uncertainty associated with the calibration method is taken as the largest deviation of $\langle R_E \rangle$ or $\langle R_P \rangle$ from unity, and is found to be less than 1% for $p_{T,\text{reco}}^{EM+JES} > 30$ GeV and less than 2% for $30 \text{ GeV} > p_{T,\text{reco}}^{EM+JES} > 20$ GeV [39].
- Uncertainty from calorimeter response** The contribution to the JES systematic from the uncertainty in the calorimeter response is derived from single particle measurements. The uncertainty in the response to charged hadrons is measured in E/p studies [40] and in testbeam data [41]. The simulation framework allows the particles in the truth jet to be associated with the energy they deposit in the calorimeter, and thus the single particle response uncertainties can be propagated to obtain an uncertainty for the response of the jet. When estimating this uncertainty,

effects relating to the calorimeter acceptance, charged particles with $E > 400\text{GeV}$, and energy deposited by neutral hadrons are also considered. Effects related to the calorimeter response are found to contribute a $1.5\% - 4\%$ uncertainty to the JES systematic.

- Uncertainty due to noise thresholds in detector simulation** The noise present in the calorimeter electronics can change over time, whereas the noise used in the simulation is fixed when the MC sample is generated. The value of the noise RMS used influences which cells are grouped into topoclusters, and thus contribute energy to the jet. The effect of the noise threshold in the simulation was measured by increasing and decreasing the noise thresholds for the topoclustering algorithm by amounts of 5-10%. The uncertainty assigned to this effect was found to be negligible for jets with $p_T > 45\text{ GeV}$, and is estimated as 1% for jets with momentum in the range $30\text{ GeV} \leq p_T \leq 45\text{ GeV}$. For jets with momentum in the range $20\text{ GeV} \leq p_T \leq 30\text{ GeV}$, the uncertainty was estimated as 1% (2%) for jets with radius 0.4 (0.6).
- Effect of additional material in simulation** As the JES calibration is intended to correct for the effects of inactive material, it is sensitive to the material description of the detector in the simulation. The effects of this were estimated by adding additional material to the simulation geometry in several places, and comparing the response obtained with the modified geometry to that obtained using the nominal geometry.
- MC event generators** The nominal MC sample used in the derivation of the JES was generated using PYTHIA, using the AMBT1 tune. Samples were also produced using ALPGEN interfaced with HERWIG and JIMMY, and using the perugia 2010 tune in PYTHIA. The ALPGEN sample used the CTEQ6.1 pdfset, and treated parton showering and hadronization effects differently to the nominal PYTHIA sample,

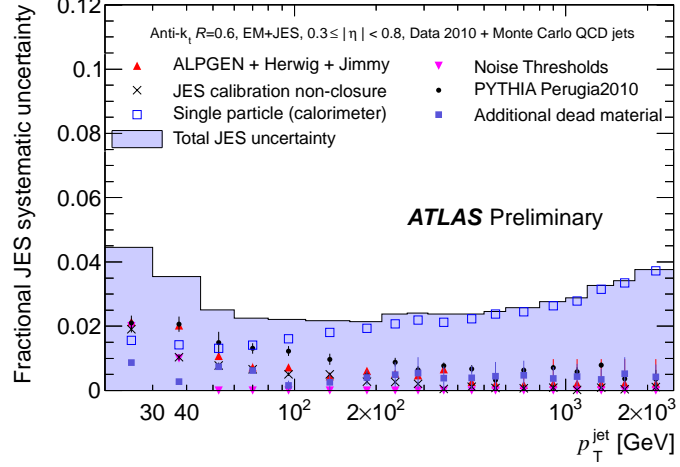
whereas the perugia2010 sample provided a different treatment of the underlying event. Deviations between the response obtained from the perugia2010 and ALPGEN +HERWIG +JIMMY samples with respect to the nominal PYTHIA sample were used to estimate the uncertainty arising from the choice of theoretical physics models.

- **Relative calibration of uncertainties between forward and central regions.** Contributions to the JES uncertainty from the above sources have been calculated in the central region, $0.3 < |\eta| < 0.8$. This uncertainty is used as a baseline, and an intercalibration method [42] is used to extend the estimate of the JES systematic into other pseudorapidity regions. This method uses a p_T balancing technique applied to dijet events in order to obtain the ratio of the calibrated jet responses in different regions of pseudorapidity. This response was calculated for data and simulation, using several different MC event generators. The RMS of the differences in response between MC and data is then added in quadrature to the baseline uncertainty, yielding the uncertainty in higher pseudorapidity regions.

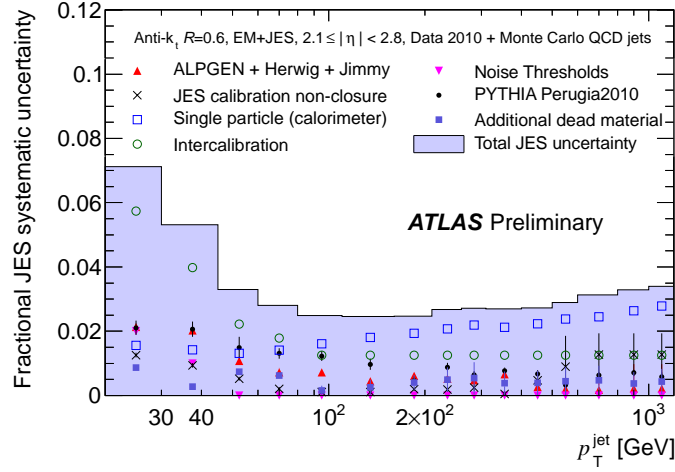
The total JES uncertainty, and its components, are plotted in figure 2.6 for $R = 0.6$ jets. The uncertainty in the calorimeter response is the dominant contribution to the JES uncertainty for jets with $p_T \geq 100$ GeV. In the central region ($0.3 < |\eta| < 0.8$), the uncertainties associated with alternative MC generators dominate below 100 GeV, while in other pseudorapidity regions intercalibration effects dominate at low p_T .

2.3.4 Jet Selection

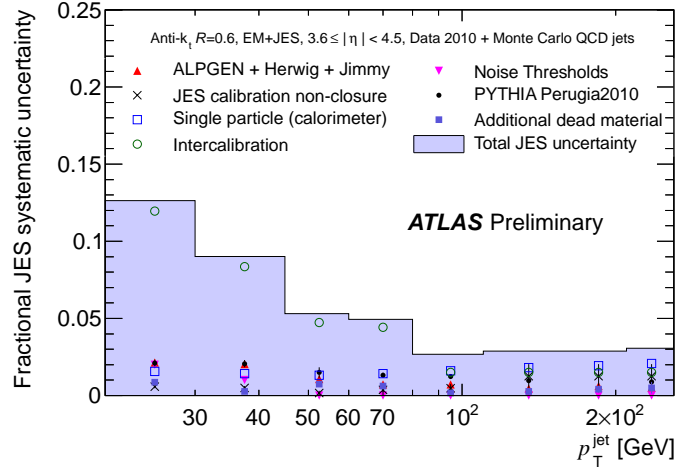
After jets have been calibrated, they are required to pass “cleaning cuts” before being included in the analysis. The cleaning cuts are intended to reject “fake” jets, which can be reconstructed from calorimeter signals that do not originate from proton proton collisions. The most significant sources of these fake jets are coherent noise in the EMB,



(a)



(b)



(c)

Figure 2.6: Systematic uncertainty on the Jet Energy Scale for jets in the regions (a) $0.3 < |\eta| < 0.8$, (b) $2.1 < |\eta| < 2.8$, (c) and $3.6 < |\eta| < 4.5$ [39]

noise bursts in the HEC, cosmic rays, and beam background events. The cleaning cuts used to reject jets are summarised below

- **Coherent noise in the EM calorimeter:** Jet candidates with $|\eta| < 2.8$ were rejected if f_{EM} , the fraction of energy deposited in the EM calorimeter, exceeded 0.9 while the LAr quality variable exceeded 0.8. The LAr quality is defined as the fraction of LAr cells in the jet which have a pulse shape significantly different to a reference shape.
- **Noise bursts (“spikes”) in the HEC:** Jet candidates were rejected if the fraction of energy deposited in the HEC was greater than $1 - \text{HECQ}$, where HECQ is the HEC quality variable and is defined analogously to the LAr quality variable. Jets were also rejected if the sum of negative energy cells exceeded 60 GeV in magnitude.
- **Cosmics rays/beam background:** Jet candidates were rejected if the average timing for jet cells was greater than 10ns from the average event time. For jets with $|\eta| < 2.0$, tracking information can be used to define the charged fraction, f_{ch} , which is the fraction of the jet p_{T} associated with tracks in the inner detector. In this case, Jets were rejected if the charge fraction was less than 0.1 and the EM fraction was less than 0.05, if the EM fraction exceeded 0.95 while the charge fraction was less than 0.05, or if 99% of the jet energy was deposited in a single layer of the calorimeter. Jets with $|\eta| > 2.0$ were rejected if the EM fraction was less than 0.05.

Jet candidates which failed these cleaning cuts were excluded from the analysis. The efficiency of these cleaning cuts towards real jets is at least 96% for jets with $p_{\text{T}} > 20$ GeV, and greater than 99% for jets with $p_{\text{T}} > 60$ GeV. In kinematic regions where the jet cleaning efficiency is less than 99%, the inefficiency is corrected for in the inclusive jet and dijet cross section measurements.

2.4 Event Selection and Data Quality

In order for an event to be considered in the inclusive jet and dijet cross section measurements, it was required to meet certain data quality criteria. These criteria were expressed in terms of Data Quality (DQ) flags. A green flag indicates that the corresponding system was operating normally, whereas a yellow flag indicates an issue that could be corrected for offline, or data that may be used with caution. Red flags are used to indicate data that are bad and should not be used.

In order for an event to be included in the inclusive jet and dijet cross section measurements, the following DQ flags were required:

- Trigger (L1Calo and L1 CTP) were required to be green. For periods G-I, the HLT flag was also required to be green
- Magnets (toroid and solenoid) were required to be green.
- Inner Detector subsystems (pixel, SCT and TRT) were required to be green.
- Track, Missing ET (from calorimeters), and Jet reconstruction performance were required to be green.
- Luminosity monitoring was required to be green.

The event was also required to have a primary vertex with at least 5 tracks. Each p_T - y bin in the analysis was associated with a particular trigger. The trigger condition for a given bin was required to be satisfied before an event could contribute jets to that bin.

These criteria were required for both the inclusive jet and dijet cross section measurements. Both of these analyses considered jets in the rapidity range $|y| < 4.4$. The inclusive jet cross section measurement considered jets with $p_T > 20$ GeV, while the measurement of the dijet mass spectrum required that the leading jet in the event have $p_T > 30$ GeV and the subleading jet have $p_T > 20$ GeV.

2.4.1 Triggers used for the inclusive jet analysis

The inclusive jet cross section measurement is performed in 7 bins of rapidity and 16 bins of p_T . A dedicated, fully efficient trigger is used to collect jets in each bin in order to maximize statistics. The three lowest p_T bins are populated using data taken from the MBTS1 (minimum bias) trigger (described in section ??). Minimum bias data from only the three earliest periods of running (A-C) were used for this purpose, as in these periods the trigger had a lower prescale (and so more data was recorded) and there was a minimal amount of pile-up. At higher p_T (above 60 GeV), data was taken using the central jet trigger for jets with $|y| < 2.8$. The rapidity bin from $2.8 < |y| < 3.6$ is referred to as the “transition bin”, as it covers the transition region between the end-cap calorimeters and the FCal (figure ??). In this region both the central and forward jet triggers were used, whereas in the forward region ($3.6 < |y| < 4.4$) only the forward jet trigger was used.

The behaviour of the jet trigger system needs to be understood it can be used effectively. This is achieved by measuring the trigger efficiency. The per-jet efficiency of a trigger represents the probability that the trigger condition will be satisfied by a given jet. It is defined as

$$\epsilon_{\text{per-jet}} = \frac{N_{\text{triggered}}}{N_{\text{reference}}}, \quad (2.6)$$

where $N_{\text{reference}}$ is the number of reconstructed jets obtained from the reference sample and $N_{\text{triggered}}$ is the number of reconstructed jets from the reference sample that satisfy the trigger condition. These quantities are binned in terms of the p_T and rapidity of the reconstructed jets, which allows the efficiency to be described as a function of these variables. For the trigger studies presented here, data taken from the minimum bias trigger (MBTS) is used to obtain the reference sample.

In order to count $N_{\text{triggered}}$, the reconstructed jets that satisfy the trigger condition need to be identified. L1 jet triggers are satisfied provided that the transverse energy deposited in a given ROI exceeds a certain threshold (as discussed in section ??). In

order to determine if a given jet satisfies the trigger condition, it must be matched to an ROI that is above the trigger threshold. A reconstructed jet is matched to an ROI from the central jet trigger if the jet lies within $\Delta R \leq 0.4$ of the ROI in $\eta - \phi$ space. The forward jet trigger relies only on data from the FCal, and the trigger towers in the FCal are summed such that there is no granularity in η . Reconstructed jets are matched to forward jet trigger ROIs if the jet lies within $\Delta\phi \leq 0.4$ of the ROI, provided the two are on the same side of the detector.

The per-jet efficiency describes the probability that the trigger will be satisfied by a given jet. However, for events containing multiple jets, only one jet needs to satisfy the trigger condition in order for all of the jets to count towards the inclusive cross section measurement. Consider an event in which there are two jets with equal and opposite momenta. If the relevant trigger has a per-jet efficiency of 90%, then each jet has a 10% chance of not satisfying the trigger condition. There is thus a 1% chance that neither jet satisfies the trigger condition, giving a 99% chance that the trigger condition is satisfied by one or both jets. For this reason, it is more appropriate to use the inclusive efficiency, ϵ_{inc} , which is given by

$$\epsilon_{\text{inc}} = \frac{N_{\text{triggered,inc}}}{N_{\text{reference}}}. \quad (2.7)$$

In this case, $N_{\text{triggered,inc}}$ is the number of jets contained in events (taken from the reference sample) in which the trigger condition is satisfied. The inclusive efficiency describes the efficiency of the trigger at the event level: if any jet in the event satisfies the trigger condition, then all jets in the event are counted. The inclusive efficiency is thus used to determine the p_{T} range in which a given trigger will be used to collect data. Trigger efficiencies for the transition and forward bins are plotted in figures 2.7 and 2.8, respectively.

In order to reduce the uncertainties on the cross section related to the trigger efficiency, triggers are only used to collect data on their “plateau” regions. The plateau point is defined by integrating bins of $N_{\text{triggered,inc}}$ and $N_{\text{reference}}$ from high p_{T} towards low p_{T} ,

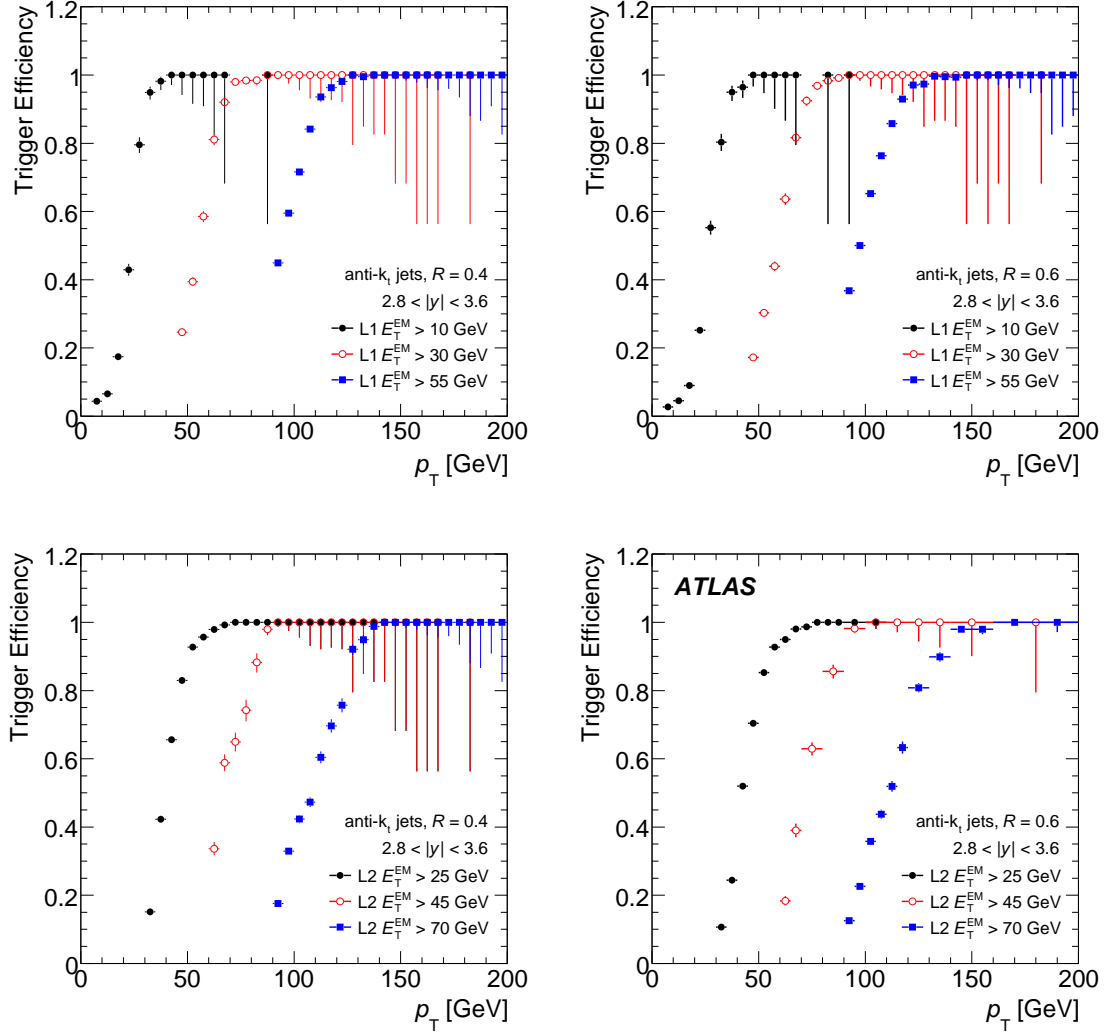


Figure 2.7: Efficiencies for L1 triggers (top) and L2 triggers (bottom) in the transition bin, for anti- k_t jets with $R=0.4$ (left) and $R=0.6$ (right).

until reaching the point where the ratio of these sums drops below 99%. The high edge of this bin is then taken as the plateau point, as the trigger is at least 99% efficient at p_T values above this point. On the plateau the trigger is treated as being fully efficient, and is used to collect data for the appropriate p_T bins.

While studying the forward jet triggers, it was observed that events containing high p_T jets in the region $3.4 < \eta < 3.9$ and $-\pi/8 < \phi < 0$ were not being selected by the trigger. The L1 trigger tower in this region was found to be producing no signal. This reduced the geometrical acceptance of the forward jet trigger by $\frac{1}{128}$, which is corrected

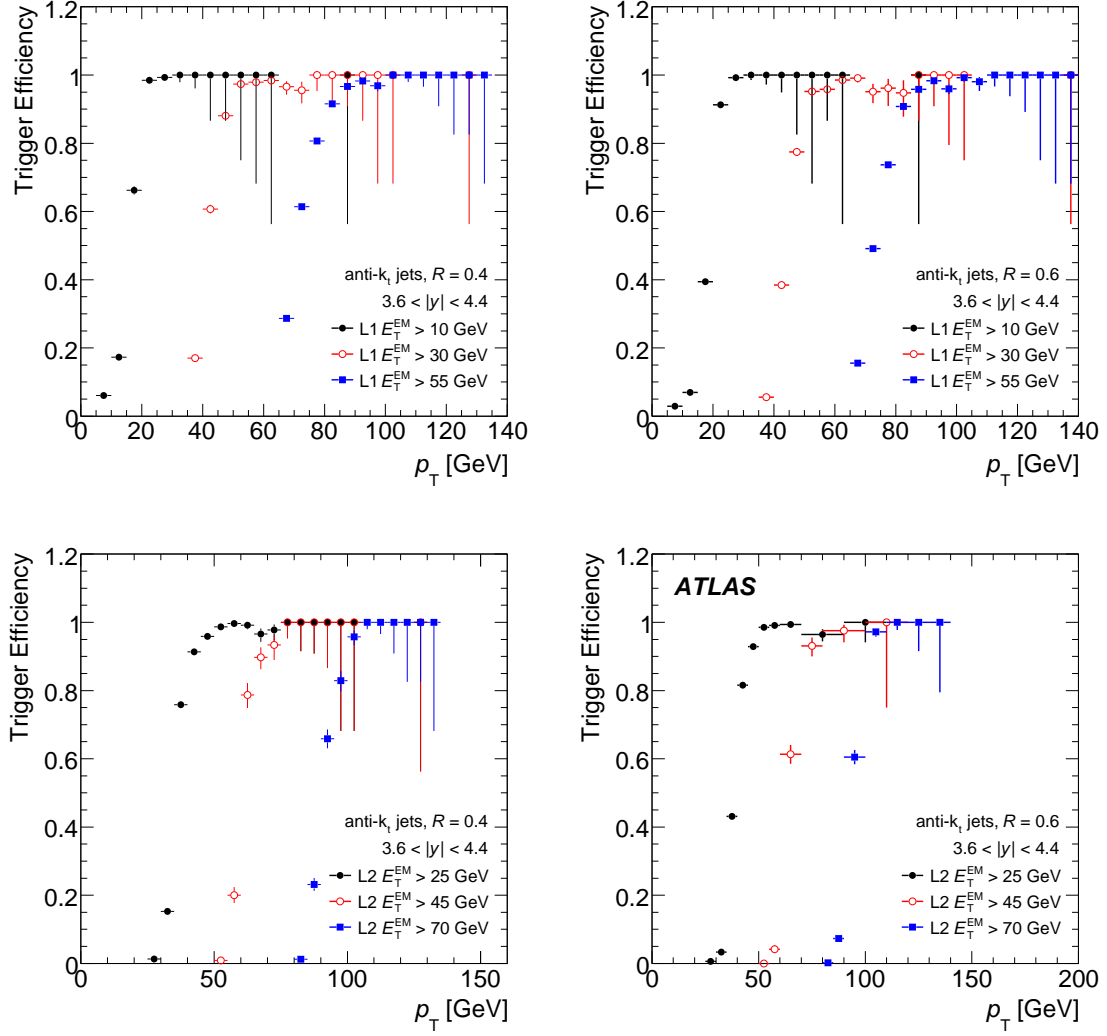


Figure 2.8: Efficiencies for L1 triggers (top) and L2 triggers (bottom) in the forward bin, for anti- k_t jets with $R=0.4$ (left) and $R=0.6$ (right).

for in the cross section calculation. Consequently, the plateau points in the forward and transition bins are defined at an efficiency of 98%. It should be noted that while the trigger tower is considered “dead”, calorimeter cells (and hence jet reconstruction) are unaffected in this region, as the cell information is read off the FEB separately from the trigger signal (as described in section ??).

As data taking progressed, the trigger system was commissioned further. The forward jet triggers were commissioned after run 161118 (period E5), and used to collect data in the forward and transition regions from then on. The HLT system was commissioned from

period G on, which allowed event rejection to occur at L2. The EF remained in “pass-through” mode throughout the remainder of 2010, meaning that all events passing at L2 were recorded. Triggers at L1 were used to collect data until the HLT was commissioned, after which L2 triggers were used (periods G-I).

2.4.2 Transition Bin

The transition bin covers the region between end-cap calorimeters and the FCal. Information from the EMEC and HEC is only used by the central jet trigger (which covers the region $|\eta| < 3.2$), while information from the FCal is only used by the forward jet trigger ($|\eta| > 3.2$). In order for the analysis to be sensitive to all jets in this region of rapidity, both the central and forward jet triggers need to be considered when collecting data. This is done by taking the logical “OR” of the two triggers, such that jets in the event are counted if either the central or forward trigger condition is met. The per-jet efficiency of each trigger throughout this rapidity range is shown in figure 2.9. The “OR” of the two triggers is fully efficient throughout the rapidity range of the transition bin, although the individual triggers are not.

When only a single trigger is used, the measured cross section is given by

$$\sigma = N_{jets} \left(\sum_i \frac{\mathcal{L}_i}{S_i} \right)^{-1}, \quad (2.8)$$

where N_{jets} is the number of jets observed and \mathcal{L}_i and S_i are the integrated luminosity and trigger prescale for the i th luminosity block, respectively. The situation is more complex in the case where two (or more) triggers are employed. In this situation we classify events as belonging to one of three classes, based on whether the event passed the forward trigger condition but not the central (case 10), the central trigger condition but not the forward (case 01), or both trigger conditions (case 11). When making these distinctions, it is important to consider whether the event satisfied a trigger condition before the prescale

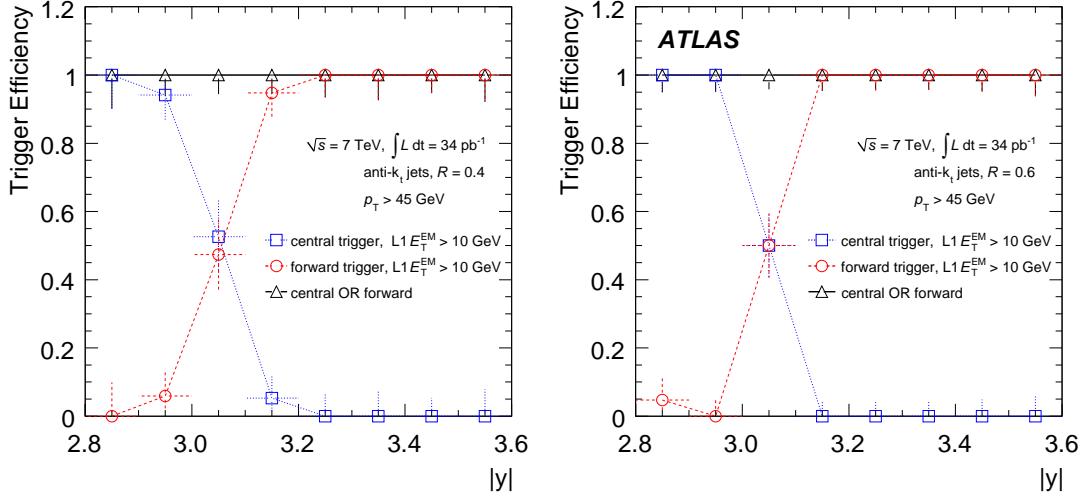


Figure 2.9: Per-jet efficiency of Level 1 forward (red) and central (blue) triggers as a function of offline jet rapidity for jets with p_T greater than 45 GeV in the transition bin ($2.8 < |y| < 3.6$), for jets with $R = 0.4$ (a) and $R = 0.6$ (b). Note that the OR of the two triggers remains fully efficient throughout the rapidity range.

was applied, as events should be classified according to the triggers that they could potentially be accepted by rather than the triggers which actually recorded the event. For L1 triggers the “Trigger Before Prescale” flag can be checked in Athena, but for L2 triggers the jets found at L2 must be checked to see if any exceed the trigger threshold.

Once the events have been divided into their respective classes, the cross section may be written as

$$\sigma = \frac{N_{01}}{\mathcal{L}_{01}} + \frac{N_{10}}{\mathcal{L}_{10}} + \frac{N_{11}}{\mathcal{L}_{11}}, \quad (2.9)$$

where integrated luminosities are given by

$$\mathcal{L}_{01} = \sum_i \frac{\mathcal{L}_i}{S_{i,01}} \quad (2.10)$$

$$\mathcal{L}_{10} = \sum_i \frac{\mathcal{L}_i}{S_{i,10}} \quad (2.11)$$

$$\mathcal{L}_{11} = \sum_i \frac{\mathcal{L}_i (S_{i,01} + S_{i,10} - 1)}{S_{i,01} S_{i,10}} \quad (2.12)$$

and $S_{i,10}$ ($S_{i,01}$) is the prescale of the forward (central) jet trigger for the i -th lumiblock.

2.4.3 Dijet Triggers

For the initial measurements made using data from ATLAS [29, 30] the dijet mass spectrum was binned in terms of the dijet mass, m_{12} , and the maximum rapidity of the two jets, $y_{\max} = \max(|y_1|, |y_2|)$. Dijet events were selected by triggering on the leading jet, using the same trigger thresholds as for inclusive analysis. These first measurements only considered cases where both jets were in the central region, with $y_{\max} < 2.8$.

When the dijet analysis was extended to cover the transition and forward regions, a new trigger scheme was considered. The intent was to bin the trigger efficiency in terms of the observables of interest. The central jet trigger would be used for $y_{\max} < 2.8$, the forward jet trigger for $3.6 < y_{\max} < 4.4$, and the OR of the two for $2.8 < y_{\max} < 3.6$, with the trigger efficiency being described by a turn-on curve in m_{12} . Each trigger could then be considered fully efficient above some threshold value for the dijet mass, and used to collect data above this point. This trigger scheme was later abandoned, as the trigger system is based on jet p_T and thus inflates the minimum dijet mass at which the trigger becomes unbiased. Consider the case where both jets in the dijet system have transverse momenta well above the trigger threshold, but the separation between jets is small. The small separation between jets will yield a small mass, and the trigger will efficiently accept dijet events in this configuration. However, in cases where the separation between jets is large and the jet momenta are close to the trigger threshold, the resulting value for the dijet mass can still be quite large while the trigger is not fully efficient. For this reason, the observables of interest were changed to m_{12} and half of the jet rapidity separation, $y^* = |y_1 - y_2|/2$. The trigger scheme then reverted back to that used for earlier versions of the analysis wherein the leading jet is used to trigger the event, although this was extended to cover the forward region. The L1 trigger efficiencies for dijet events are plotted as a function of the leading jet p_T in figures 2.10 and 2.11, for the transition

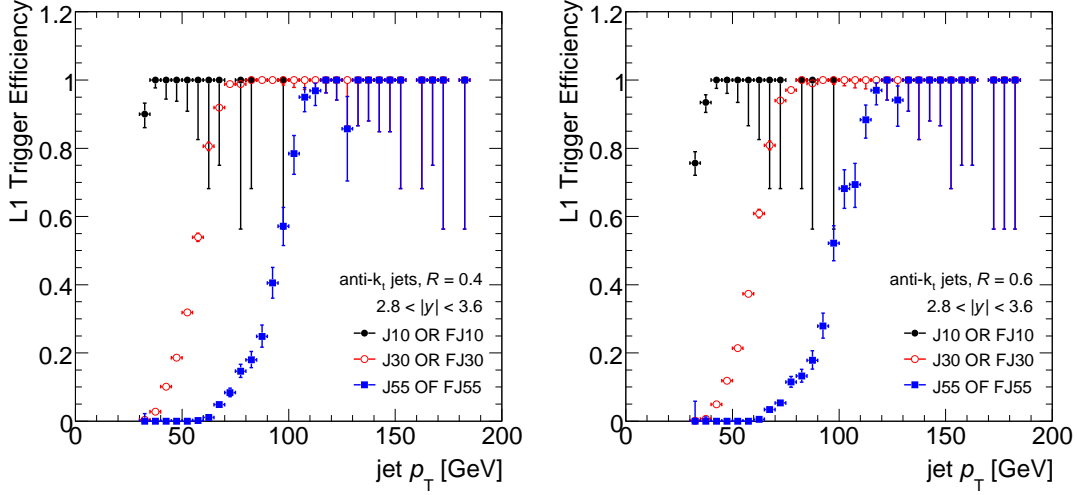


Figure 2.10: L1 trigger efficiencies for dijet events in which the leading jet lies in the transition bin, for anti- k_t jets with $R = 0.4$ (left) and $R = 0.6$ (right).

bin and forward bin respectively. The trigger scheme was then expanded to consider the subleading jet, utilizing a method similar to what was done for the transition bin in the inclusive analysis. The kinematic region is divided into a number of bins in p_T and rapidity, each of which is associated with a trigger threshold. Events are then divided into categories based on whether the trigger condition associated with the leading jet was met, or that for the the subleading jet, or if both trigger conditions were satisfied. As there is some overlap between the forward and central jet triggers in the region $3.0 < |y| < 3.2$ (fig 2.9), jets in this region are matched to ROI words at L1 or trigger jets at L2 in order to determine whether the jet should be associated with forward or central trigger. Events are then weighted based on the prescales of the triggers, using a generalized version of the method described in section 2.4.2, in order to account for the larger number of trigger categories.

2.5 Unfolding

After the cross section calculations have been carried out as described above, the data needs to be corrected in order to account for acceptance and detector effects before it can

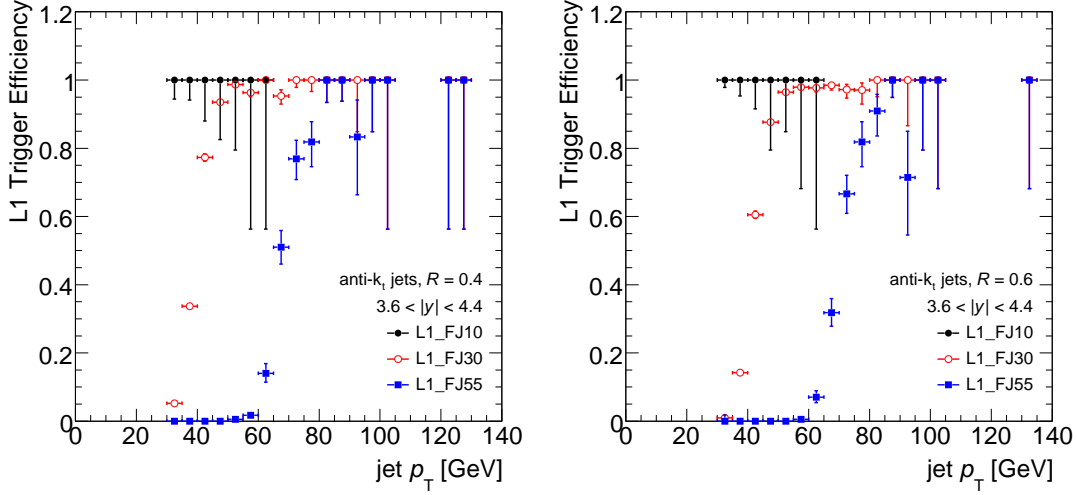


Figure 2.11: L1 trigger efficiencies for dijet events in which the leading jet lies in the forward bin, for anti- k_t jets with $R = 0.4$ (left) and $R = 0.6$ (right).

be compared to any theoretical predictions. As the jet cross section falls sharply with p_T , the non-zero resolution of the detector causes the measured spectrum to be skewed towards higher p_T relative to the “true” spectrum. Monte Carlo may be used to compare the p_T of truth jets with reconstructed jets in order to understand the effects of the detector resolution. These effects can then be “unfolded” from the measured spectrum in order to obtain the spectrum of jets prior to their interaction with the detector.

Information on detector related effects is contained in the transfer matrix, A_{ij} . The transfer matrix describes the influence that detector effects have on the measured results, and must be derived from simulation. The entry A_{ij} is equal to the number of truth jets in the j -th p_T bin which are then reconstructed in the i -th p_T bin. This may be normalized to produce the folding matrix of probabilities, P_{ij} , given by

$$P_{ij} = \frac{A_{ij}}{\sum_{k=0}^{N_b} A_{kj}} \quad (2.13)$$

The spectrum at truth level, t_j , and the reconstructed spectrum r_j , are then related by

$$r_j = \sum_{k=0}^{N_b} P_{jk} t_k. \quad (2.14)$$

An unfolded result, u_j , may then be obtained from the measured data d_j , by solving the matrix equation

$$d_j = \sum_{k=0}^{N_b} P_{jk} u_k. \quad (2.15)$$

The solution to this may be found by inverting P_{ij} , such that $u_j = \sum_k P_{ik}^{-1} d_k$. However, this is undesirable as it yields large fluctuations in u_j [43]. Transfer matrices tend to have large condition numbers, meaning that the solution is sensitive to slight changes in the input. Small variations in d_j , which may be due to statistical fluctuations, can produce large spurious fluctuations in u_j .

In order to avoid this, the unfolding method must incorporate some form of regularization. Typically equation 2.15 is solved numerically, and regularization may be done, for example, by incorporating the smoothness of u_j into the optimization method [43]. In this analysis, the unfolding is carried out using the Iterative, Dynamically Stabilized (IDS) method [44, 45], which is described below.

2.5.1 IDS method

In the IDS method, the MC is re-weighted at each iteration such that the reconstructed MC spectrum is brought closer to that of the measured data, with the truth level spectrum and the transfer matrix adjusted accordingly. As the reconstructed MC is brought closer to the measured data spectrum through re-weighting, the truth level spectrum approaches the desired unfolded result. Any differences between the measured data spectrum and the reweighted reconstructed MC spectrum are then unfolded.

Regularization is implemented through the use of a regularization function, $f(\Delta x, \sigma, \lambda)$.

This function determines how much unfolding should be carried out in a given iteration based on the difference between data and Monte Carlo, Δx , the uncertainty in this difference, σ , and a regularization parameter λ . The regularization function should take the ratio $\Delta x/\sigma\lambda$ as an argument, and return a value near zero at small values of this argument and approach one at higher values.

As the regularization function depends on the difference between data and Monte Carlo, it is important that the Monte Carlo be normalized appropriately. The discrepancy is defined as

$$\Delta d_k = d_k - \frac{N_{\text{dSmc}}}{N_{\text{MC}}} r_k \quad (2.16)$$

where N_{MC} is the total number of jets in the MC sample and N_{dSmc} is the number of jets in the data spectrum that correspond to structures/shapes in the MC spectrum. Normalizing the MC in this way enables the unfolding to preserve features in the data, such as new physics signals, which were not simulated in the MC, while correctly scaling the MC in regions where it has a similar shape to the data. The total number of jets in the data sample may be taken as an initial estimate for N_{dSmc} . A better estimate may then be obtained using

$$N'_{\text{dSmc}} = N_{\text{dSmc}} + \sum_{k=1}^{N_B} (1 - f(\Delta d, \sigma, \lambda)) \Delta d_k. \quad (2.17)$$

This procedure may be repeated until the relative change in N_{dSmc} is less than a desired threshold.

2.5.2 Matching Efficiency

In order to obtain the transfer matrix from the Monte Carlo, reconstructed jets need to be matched with a corresponding truth jet. Jets are matched if they lie within a distance $\Delta R < 0.3$ in $y - \phi$ space. The spectrum of matched truth (or reconstructed) jets may be obtained by projecting the transfer matrix on the appropriate axis. The

matched spectrum may then be compared to the unmatched spectrum to obtain the matching efficiency for truth jets and for reconstructed jets. As the transfer matrix is derived using only matched pairs of jets, the effect of the matching efficiency should be taken into consideration. Prior to the unfolding the measured data is multiplied by the matching efficiency for reconstructed jets, and after unfolding the result is divided by the matching efficiency for truth jets.

An initial unfolding may then be performed on the data, yielding the result

$$u_j = t_j \cdot \frac{N_{\text{dSmc}}}{N_{\text{MC}}} + [1 - f(\Delta d_k, \sigma d_k, \lambda_M)] \cdot \Delta d_j + \sum_{k=1}^{N_B} f(\Delta d_k, \sigma d_k, \lambda_M) \cdot \tilde{P}_{kj} \cdot \Delta d_k \quad (2.18)$$

where the unfolding matrix \tilde{P}_{ij} is obtained from the transfer matrix:

$$\tilde{P}_{ij} = \frac{A_{ij}}{\sum_{k=0}^{N_b} A_{ik}} \quad (2.19)$$

The regularization functions determine how much unfolding is done in a given bin, based on the regularization parameter λ and significance of Δd_k . Only the difference between measured data and reconstructed MC is unfolded: In bins where Δd_k is small the unfolded result is dominated by the truth level MC spectrum. In those bins where the discrepancy is significant, the regularization parameter λ determines how much unfolding is carried out. As λ increases, less unfolding is performed on the data.

Once an initial estimate of u_j has been obtained, this may be used to re-weight the MC at truth level, and thus improve the transfer matrix. The updated transfer matrix is given by

$$A'_{ij} = A_{ij} + f(|\Delta u_j|, \sigma u_j, \lambda_M) \cdot \frac{N_{\text{MC}}}{N_{\text{dSmc}}} \cdot P_{ij} \cdot \Delta u_j, \quad (2.20)$$

where

$$\Delta u_j = u_j - \frac{N_{\text{dSmc}}}{N_{\text{MC}}} \cdot t_j. \quad (2.21)$$

The new transfer matrix can then be used to update the folding and unfolding matrices,

P_{ij} and \tilde{P}_{ij} .

The procedure may then be carried out iteratively in the following sequence

- Update the normalization factor, N_{dSmc} , according to 2.17.
- Perform the unfolding.
- Use the unfolded data to update the transfer matrix, and the folding/unfolding matrices.

2.6 Treatment of uncertainties

2.6.1 Statistical uncertainties

The statistical uncertainties on the final (unfolded) cross section measurement are obtained through “toy” Monte Carlos. For each toy, Poisson fluctuations are applied to the measured data spectrum and to the transfer matrix. The fluctuated data is then unfolded using the fluctuated transfer matrix. The unfolded spectra from the toys are then used to compute a covariance matrix, from which the statistical uncertainty on the unfolded data is taken.

2.6.2 Systematic Uncertainties

The JES uncertainty is the dominant source of systematic uncertainty. Its effect on the final cross section result is found by propagating each of the JES components listed in section 2.3.3 through the unfolding procedure.

The uncertainty on the cross section associated with a given component is obtained using Monte Carlo. For each rapidity bin of the MC spectrum, a modified spectrum is obtained by shifting the jet p_{Tup} by one standard deviation of the JES uncertainty component being considered. A second modified spectrum is obtained by shifting jets

down in p_T by the same amount. These modified spectra are then unfolded using the same technique as for data. The relative difference between the modified and nominal spectra (after unfolding) is then taken as the uncertainty on the cross section associated with this JES component.

The effect of the jet energy resolution (JER) uncertainty is propagated through the unfolding in a similar fashion to the JES uncertainty. A modified Monte Carlo sample is produced by smearing the p_T of the reconstructed jets in the nominal MC sample. The reconstructed jets have their p_T smeared by a factor Δ , where Δ is a random variable with standard deviation σ_Δ and a mean of one. The standard deviation of Δ is chosen to satisfy

$$\sigma_\Delta^2 + \sigma_{\text{nom}}^2 = (\sigma_{\text{nom}} + \sigma_{\text{JER}})^2, \quad (2.22)$$

where σ_{nom} is the nominal JER and σ_{JER} is its uncertainty. The additional smearing is thus applied in such a way as to increase the effective JER by one standard deviation. The data is then unfolded using the modified transfer matrix, and the difference between this result and that unfolded with the nominal transfer matrix is taken as the systematic uncertainty.

The matching between truth and reconstructed jets is another source of systematic uncertainty. As mentioned earlier, the transfer matrix is constructed by matching truth and reconstructed jets within $\Delta R < 0.3$ in rapidity and azimuthal angle. Transfer matrices are also constructed by matching jets within $\Delta R < 0.4$ and $\Delta R < 0.2$. The unfolding is carried out using these matrices, and the largest difference between either result and that obtained from the nominal transfer matrix is taken as the uncertainty.

Shape variations between the MC spectrum and the data will also introduce systematic uncertainty through the unfolding procedure. To estimate this effect, the truth level MC spectrum is reweighted in such a way to improve the agreement between the reconstructed MC and the measured data. The reweighted MC is then unfolded using the original transfer matrix (i.e., the one used to unfold the data). The difference between

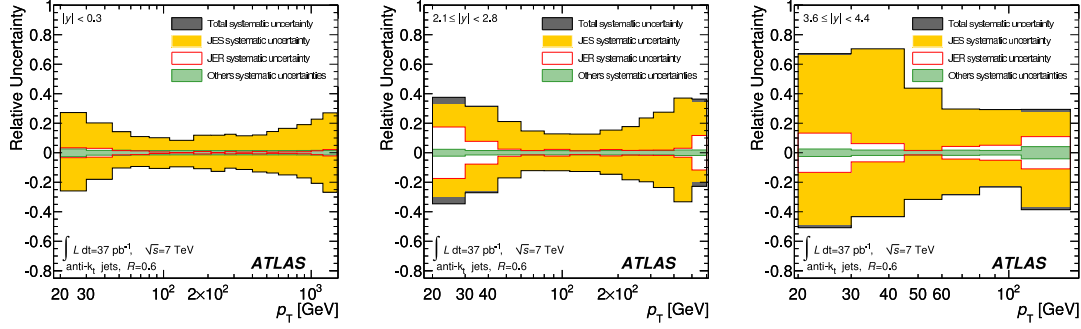


Figure 2.12: Systematic uncertainty on the inclusive jet cross section for anti- k_t jets with $R = 0.6$, for jets with rapidities of (a) $0.3 < |y| < 0.8$, (b) $2.1 < |y| < 2.8$, and (c) $3.6 < |y| < 4.4$.

the result of this and the reweighted truth level MC is taken as a systematic uncertainty, as it reflects the effect of the MC shape on the unfolded spectrum.

The efficiency with which jets are reconstructed has also been considered. This is equivalent to the matching efficiency in the Monte Carlo, and may be estimated in the data by matching reconstructed jets to track jets defined using information from the inner detector. These two efficiencies may be compared in order to estimate the degree to which the jet reconstruction efficiency is mis-modeled by the simulation. The difference is taken as a systematic uncertainty, and is less than 1% for jets with p_T above 30 GeV.

The relative systematic uncertainty for selected rapidity regions is plotted in figure 2.12, showing the contributions from various components.

2.7 Results and discussion

2.7.1 Inclusive Jet Cross Section

Results for the inclusive jet cross section are plotted in figure 2.13 for $R = 0.4$ jets and figure 2.14 for $R = 0.6$. Theoretical predictions are obtained using NLOJET++ with the CT10 pdf set. Two of the parameters used by the event generator are the factorization scale μ_f and the normalisation scale mu_r . The normalisation scale describes the scale at

which α_s is evaluated, while the factorisation scale describes the scale at which the PDFs are sampled. For the theoretical predictions of the inclusive jet cross section, both of these scales have been set to the p_T of the leading jet: $\mu_r = \mu_f = p_T^{\max}$.

The NLOJet++ calculates (at NLO) the cross section for partons produced in the hard scattering. Before this may be compared to data, it must be corrected for non-perturbative QCD effects (i.e. hadronization and underlying event effects). This correction is derived from PYTHIA. Pythia is run normally, using an LO matrix element for the hard scattering before showering the incoming/outgoing partons and incorporating hadronisation and UE effects. It is also run with the hadronisation and UE calculations turned off, essentially giving a parton level cross section at LO. A correction factor, C_{NP} is then obtained by taking the ratio of these two results, such that

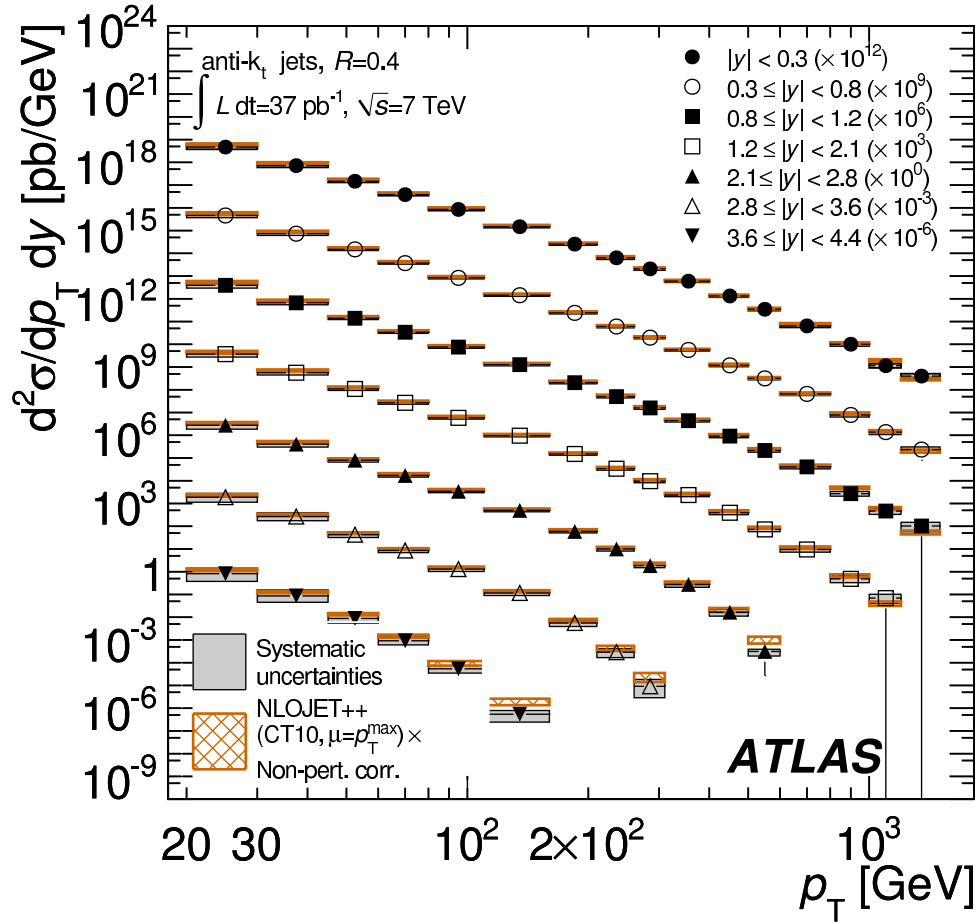
$$C_{\text{NP}} = \frac{\sigma_{\text{full}}}{\sigma_{\text{sans-UE/had}}}, \quad (2.23)$$

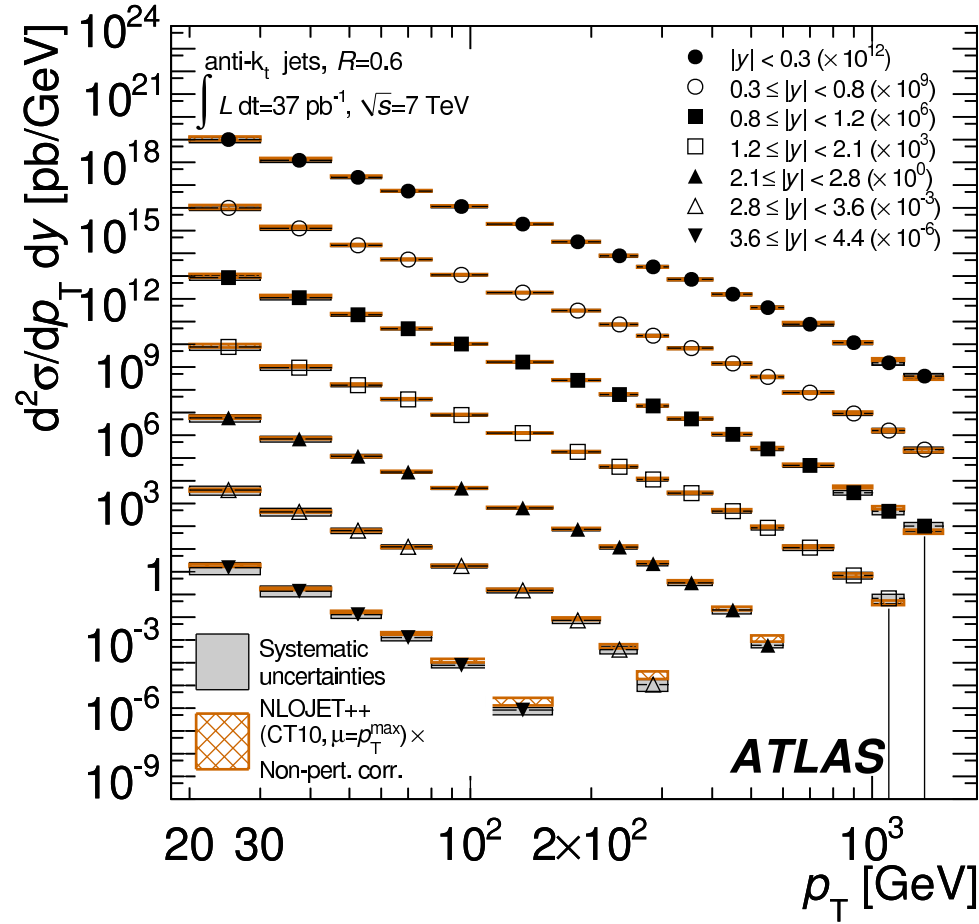
where $\sigma_{\text{sans-UE/had}}$ is the cross section obtained from pythia with hadronisation and UE calculations turned off and σ_{full} is the cross section obtained from pythia with these effects enabled. The correction factor C_{NP} is computed bin by bin in p_T and y , and multiplied by NLOJet++ result to obtain the theoretical prediction for the cross section with non-perturbative effects included. The agreement between data and theory is generally good.

In figures 2.15 ($R = 0.4$) and 2.16 ($R = 0.6$), the ratio of the data and theory results is plotted. The CT10 pdf set is used as a baseline, such that cross sections are plotted relative to that obtained from NLOJet++ with CT10. Theoretical results obtained using NLOJet++ with other pdf sets (MSTW2008, NNPDF 2.1, and HERAPDF 1.5) are also shown. NLOjet++ tends to predict a higher cross section than that seen in data when using any of the pdf sets considered here, with the discrepancy worse at high p_T or high rapidity. MSTW2008 tends to follow the data better in these regions. In all cases, the differences between data and theory are similar in magnitude to the systematic

uncertainties from theory and data.

Figures 2.17 and 2.18 again show the ratio of the data and theory results, but also include theoretical results obtained from POWHEG. In these cases, POWHEG is used to compute the matrix element for the hard scattering at NLO using the CT10 PDF set, and is interfaced to either PYTHIA (with either the AUET2B or Perugia2011 tune) or HERWIG (AUET tune). In these cases, POWHEG interacts with the parton shower event generators in such a way that NLO accuracy is maintained throughout the calculation. The pink curves in figures 2.17 and 2.18 show the results obtained from POWHEG when it is run with the hadronisation and underlying event calculations switched off, with non perturbative corrections applied in the same manner used for NLOJet++ as discussed above. The POWHEG results vary significantly depending on the method used for parton showering. These variations are on the order of 30%, whereas the theoretical uncertainty due to non-perturbative effects is less than 10% for jets with $R = 0.4$. The results obtained by interfacing POWHEG with the AUET2B tune of pythia show fairly good agreement with the data over the entire kinematic range studied.

Figure 2.13: Inclusive jet cross section for ant-kt jets with $R = 0.4$.

Figure 2.14: Inclusive jet cross section for ant-kt jets with $R = 0.6$.

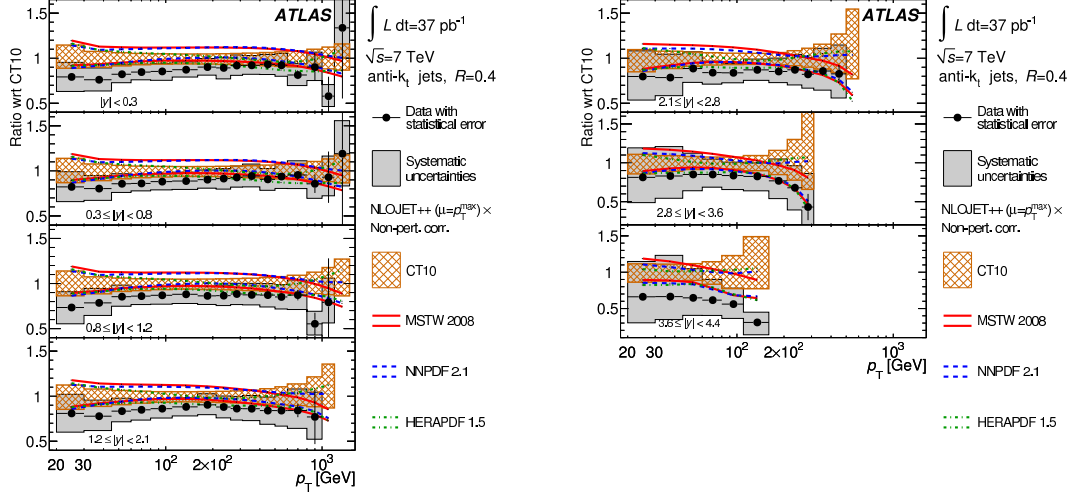


Figure 2.15: Ratio of the inclusive jet cross section to the CTEQ10 prediction, for different rapidity bins using anti- k_t jets with $R = 0.4$. Other pdfs also shown.

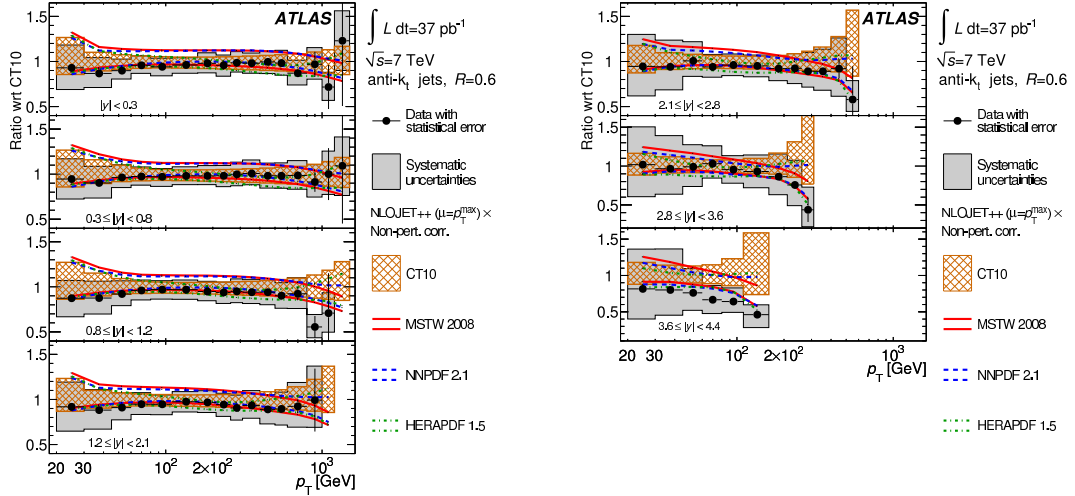


Figure 2.16: Ratio of the inclusive jet cross section to the CTEQ10 prediction, for different rapidity bins using anti- k_t jets with $R = 0.6$. Other pdfs also shown.

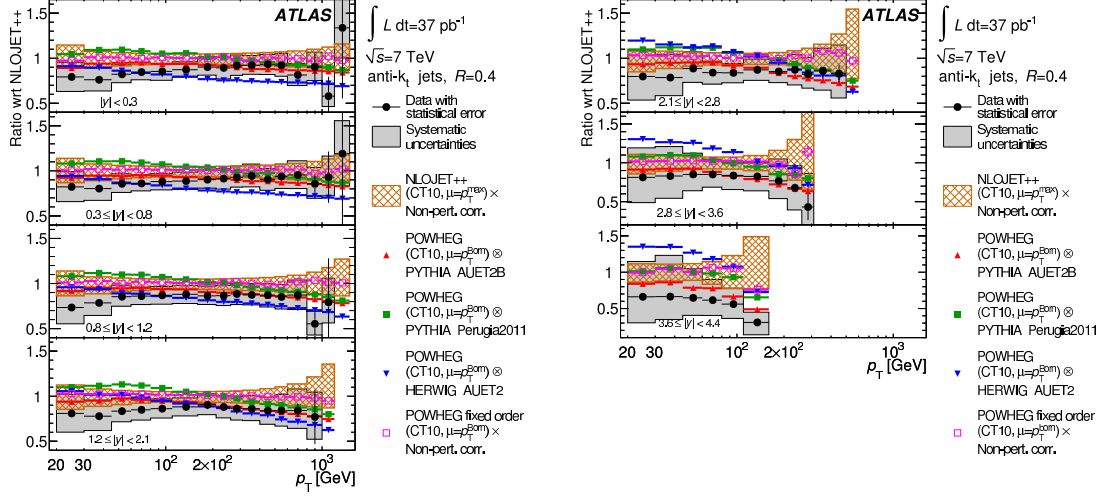


Figure 2.17: Ratio of the inclusive jet cross section to the CT10 prediction, for different rapidity bins using anti- k_t jets with $R = 0.4$. Theoretical predictions made using POWHEG are also shown.

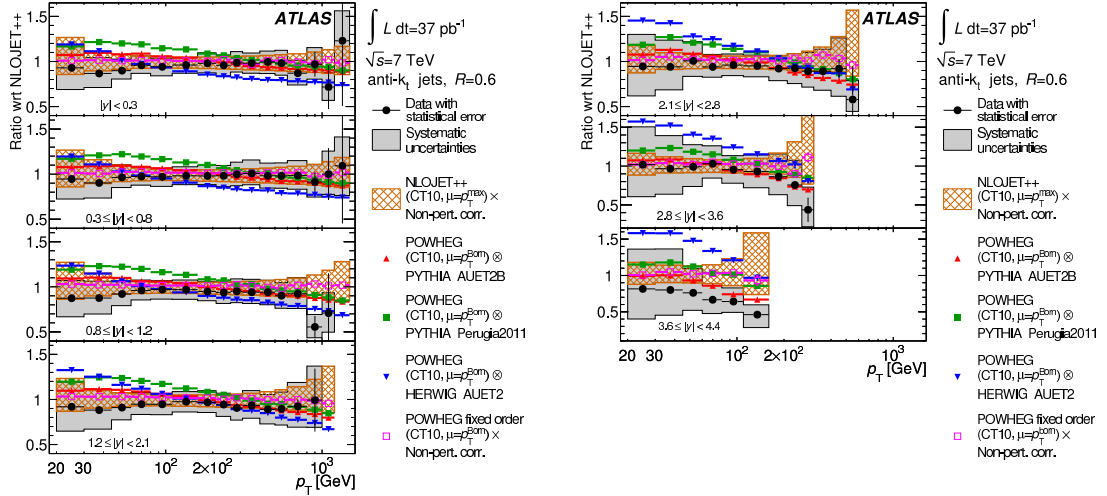


Figure 2.18: Ratio of the inclusive jet cross section to the CT10 prediction, for different rapidity bins using anti- k_t jets with $R = 0.6$. Theoretical predictions made using POWHEG are also shown.

2.7.2 Dijet Mass Spectrum

The dijet mass spectrum, after unfolding, is plotted in figures 2.19 for jets with $R = 0.4$, and 2.20 for $R = 0.6$. The theoretical results are again obtained using NLOJET++ with the CT10 pdf set and non-perturbative corrections obtained from PYTHIA. In this case, the scales

$$\mu_r = \mu_f = \frac{m_{12}}{2 \cosh(0.7y^*)} \quad (2.24)$$

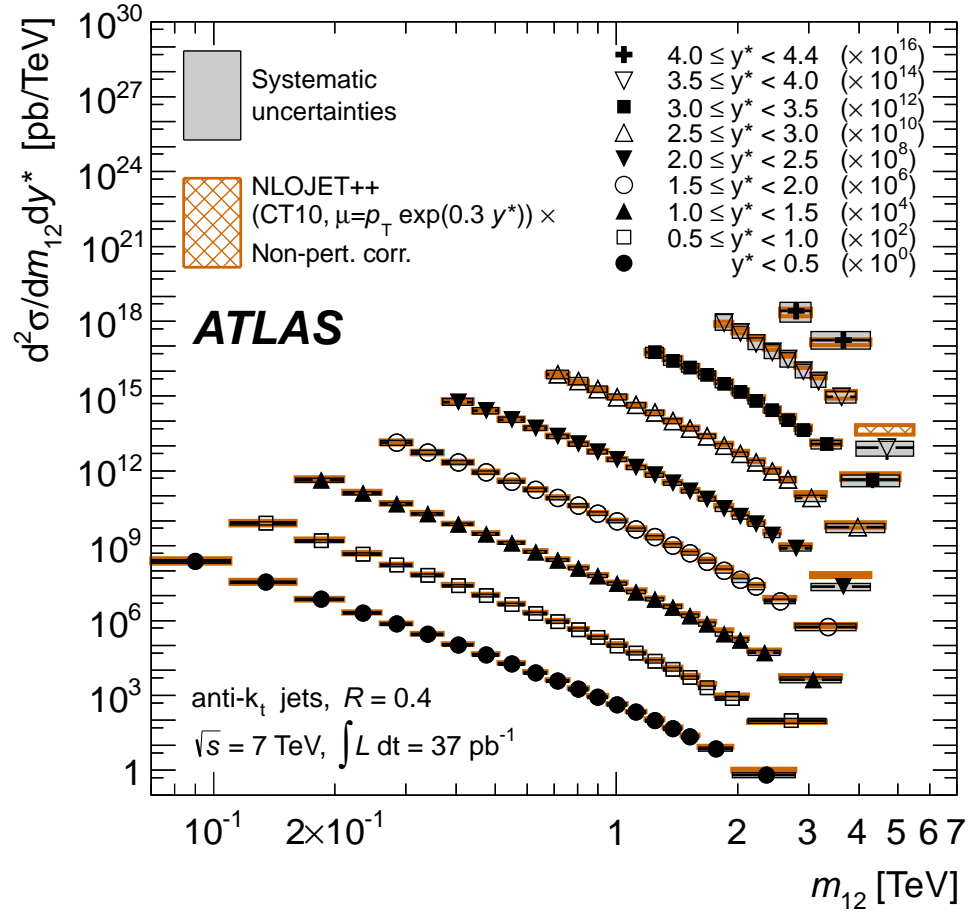
were chosen for normalization and factorization, as this choice was found to be more stable at high values of y^* .

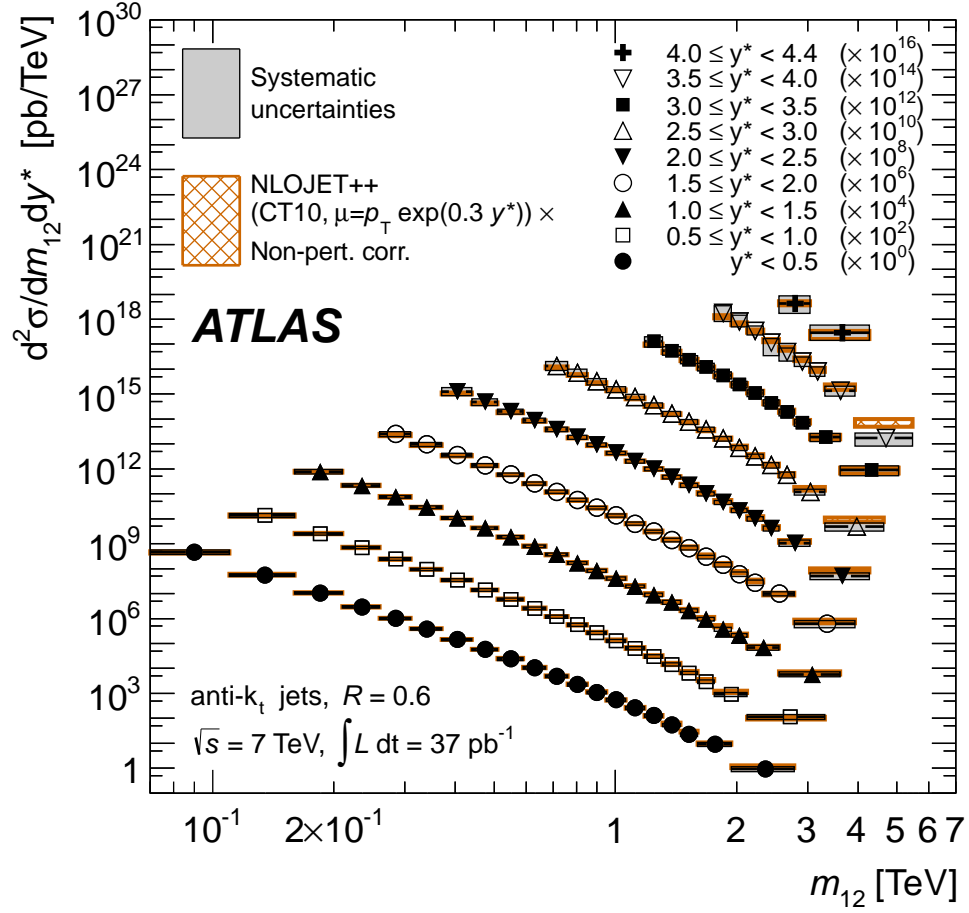
Theoretical results from different pdf sets are plotted in figures 2.21 and 2.22, shown as a ratio to the result obtained using CT10. Data and theory can be seen to agree well at small separations. At larger values of y^* , fluctuations appear in the data/theory ratio. The data spectrum is smooth in this region, and fluctuations are due to lack of statistics in the theoretical predictions.

Results obtained from POWHEG are plotted in figures 2.23 and 2.24. POWHEG did not exhibit the instabilities seen in the NLOJet++ results at high values of y^* , and so the scales $\mu_r = \mu_f = p_T^{\max}$ are again used with POWHEG. The best agreement between theory and data is seen when using the AUET2B tune, with Perugia2011 and AUET yielding cross sections higher than that seen in data.

2.8 Summary

The inclusive jet and dijet cross sections have been measured with 37pb^{-1} of data recorded in 2010. These measurements represent a coherent QCD measurement made over a large kinematic region, with a degree of precision in the forward region that has not previously been reached at a hadron-hadron collider.

Figure 2.19: Dijet mass spectrum for ant-kt jets with $R = 0.4$.

Figure 2.20: Dijet mass spectrum for ant-kt jets with $R = 0.6$.

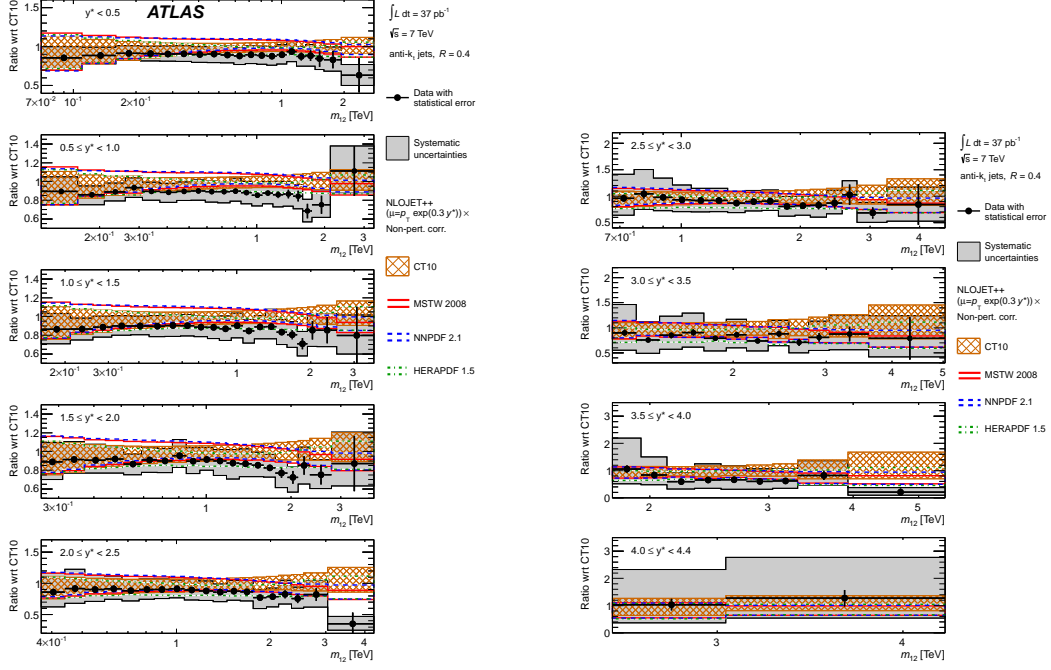


Figure 2.21: Ratio of measured dijet mass spectrum to theoretical prediction obtained using POWHEG, for anti- k_t jets with $R = 0.4$.

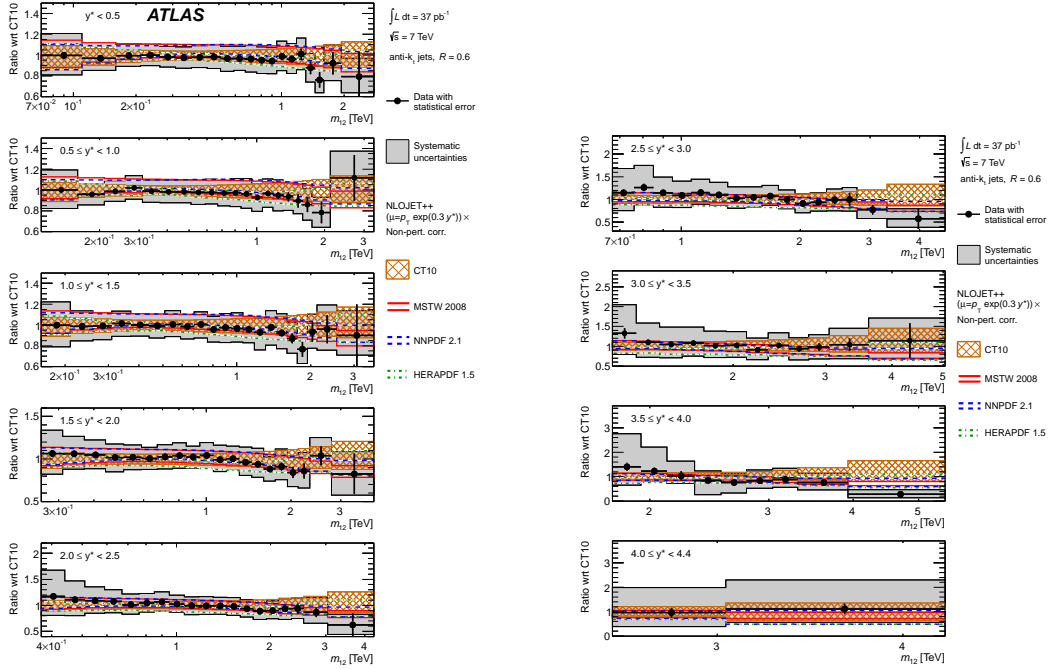


Figure 2.22: Ratio of measured dijet mass spectrum to theoretical prediction obtained using POWHEG, for anti- k_t jets with $R = 0.6$.

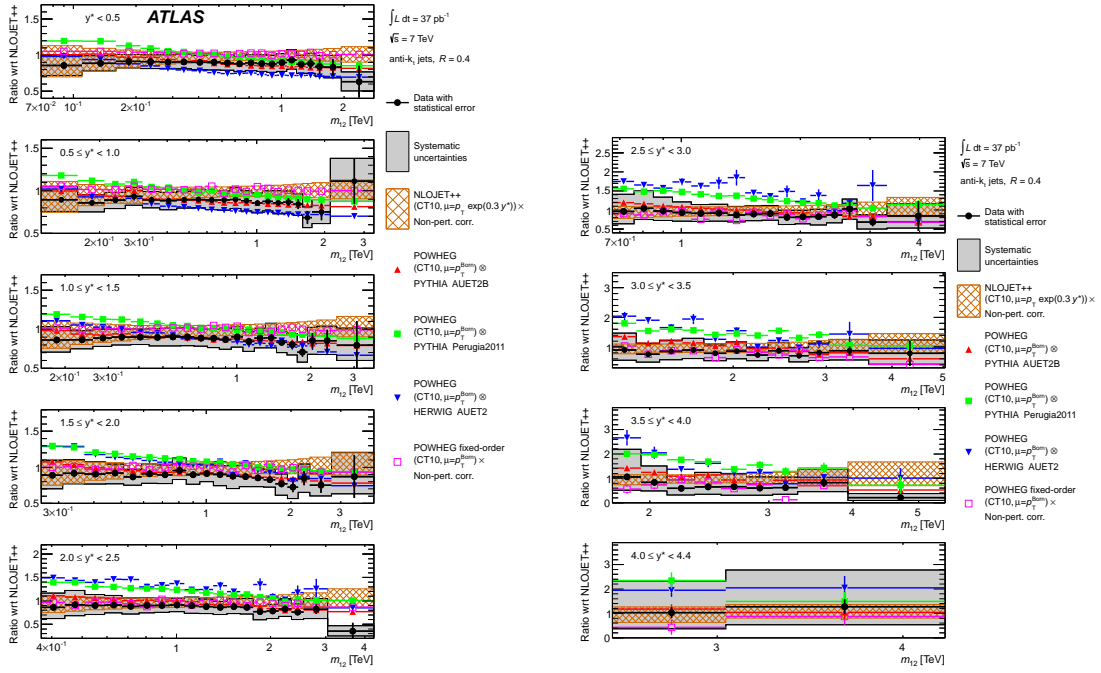


Figure 2.23: Ratio of measured dijet mass spectrum to theoretical prediction obtained using POWHEG, for anti- k_t jets with $R = 0.4$.

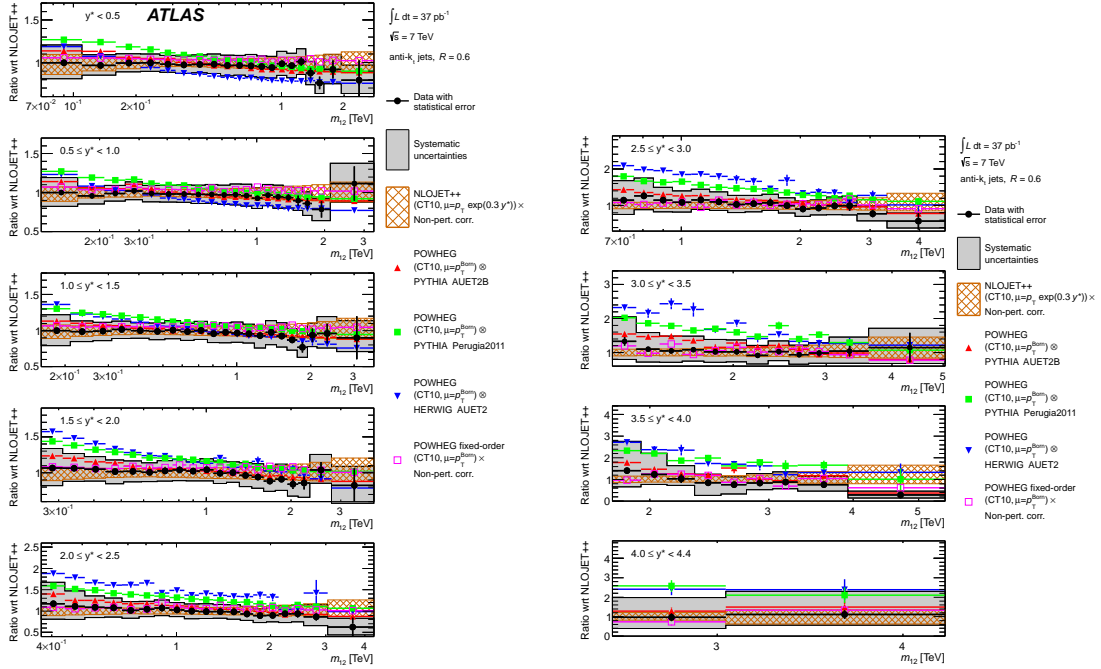


Figure 2.24: Ratio of measured dijet mass spectrum to theoretical prediction obtained using POWHEG, for anti- k_t jets with $R = 0.6$.

Bibliography

- [1] S. Behrends et al. Observation of Exclusive Decay Modes of B Flavored Mesons. *Phys.Rev.Lett.*, 50:881–884, 1983.
- [2] G. Arnison et al. Experimental Observation of Lepton Pairs of Invariant Mass Around $95\text{-GeV}/c^{*2}$ at the CERN SPS Collider. *Phys.Lett.*, B126:398–410, 1983.
- [3] G. Arnison et al. Experimental Observation of Isolated Large Transverse Energy Electrons with Associated Missing Energy at $s^{*}(1/2) = 540\text{-GeV}$. *Phys.Lett.*, B122:103–116, 1983.
- [4] CERN. CERN experiments observe particle consistent with long-sought Higgs boson, 2012. <http://press.web.cern.ch/press/PressReleases/Releases2012/PR17.12E.html>.
- [5] G. Aad et al. Observation of a new particle in the search for the Standard Model Higgs boson with the ATLAS detector at the LHC. *Physics Letters B*, 716(1):1 – 29, 2012.
- [6] J. Beringer et al. Review of particle physics. Particle Data Group. *Phys. Rev.*, D86, 2012.
- [7] John C. Collins, Davison E. Soper, and George Sterman. Factorization for short distance hadron-hadron scattering. *Nuclear Physics B*, 261(0):104 – 142, 1985.
- [8] C.P. Burgess and G.D. Moore. *The Standard Model: A Primer*. Cambridge University Press, 2007.

- [9] W. Greiner, S. Schramm, and E. Stein. *Quantum Chromodynamics*. Springer, 2007.
- [10] G. Altarelli and G. Parisi. Asymptotic freedom in parton language. *Nuclear Physics B*, 126(2):298 – 318, 1977.
- [11] Hung-Liang Lai et al. New parton distributions for collider physics. *Phys.Rev.*, D82:074024, 2010.
- [12] The Electron-Proton Collider Hera. *Annual Review of Nuclear and Particle Science*, 44:413–452, 1994.
- [13] L.M. Lederman. The Tevatron. *Sci.Am.*, 264:26–33, 1991.
- [14] Hung-Liang Lai et al. CT10 global analysis, additional figures and results, 2012. <http://hep.pa.msu.edu/cteq/public/ct10/figs/>.
- [15] J M Campbell, J W Huston, and W J Stirling. Hard interactions of quarks and gluons: a primer for LHC physics. *Reports on Progress in Physics*, 70(1):89, 2007.
- [16] S. Catani and M.H. Seymour. A General algorithm for calculating jet cross-sections in NLO QCD. *Nucl.Phys.*, B485:291–419, 1997.
- [17] Paolo Nason. A new method for combining NLO QCD with shower Monte Carlo algorithms. *Journal of High Energy Physics*, 2004(11):040, 2004.
- [18] Torbjörn Sjöstrand, Stephen Mrenna, and Peter Skands. A brief introduction to PYTHIA 8.1. *Computer Physics Communications*, 178(11):852–867, 2008.
- [19] G. Corcella et al. HERWIG 6.5 release note. 2002.
- [20] Torbjorn Sjostrand. Monte Carlo Generators. pages 51–74, 2006.
- [21] Stefano Frixione and Bryan R. Webber. Matching NLO QCD computations and parton shower simulations. *JHEP*, 0206:029, 2002.

- [22] J. Butterworth et al. Jimmy generator: multiparton interactions in HERWIG, 2012.
<http://jimmy.hepforge.org/>.
- [23] Further ATLAS tunes of PYTHIA6 and Pythia 8. 2011.
- [24] Peter Zeiler Skands. Tuning Monte Carlo Generators: The Perugia Tunes. *Phys.Rev.*, D82:074018, 2010.
- [25] Stefano Frixione, Paolo Nason, and Carlo Oleari. Matching NLO QCD computations with Parton Shower simulations: the POWHEG method. *JHEP*, 0711:070, 2007.
- [26] Zoltan Nagy. NLOJET++ home page, 2012.
<http://www.desy.de/~znagy/Site/NLOJet++.html>.
- [27] Simone Alioli et al. A general framework for implementing NLO calculations in shower Monte Carlo programs: the POWHEG BOX. *JHEP*, 1006:043, 2010.
- [28] Simone Alioli et al. Jet pair production in POWHEG. *JHEP*, 1104:081, 2011.
- [29] ATLAS Collaboration. Measurement of inclusive jet and dijet cross sections in proton-proton collisions at 7 TeV centre-of-mass energy with the ATLAS detector. 2010.
- [30] ATLAS Collaboration. Measurement of jet production in 7 TeV proton-proton collisions with the ATLAS Detector. Technical Report ATLAS-COM-CONF-2010-052, CERN, Geneva, Jun 2010. See back up note for full author list.
- [31] Measurement of inclusive jet and dijet cross sections in proton-proton collision data at 7 TeV centre-of-mass energy using the ATLAS detector. Technical Report ATLAS-CONF-2011-047, CERN, Geneva, Mar 2011.
- [32] Georges Aad et al. Measurement of inclusive jet and dijet production in pp collisions at $\sqrt{s} = 7$ TeV using the ATLAS detector. *Phys. Rev.*, D86:014022, 2012.

- [33] Serguei Chatrchyan et al. Measurement of the Inclusive Jet Cross Section in pp Collisions at $\sqrt{s} = 7$ TeV. *Phys.Rev.Lett.*, 107:132001, 2011.
- [34]
- [35] Matteo Cacciari, Gavin P. Salam, and Gregory Soyez. The $anti k_t$ jet clustering algorithm. *JHEP*, 04:063, 2008.
- [36] Dokshitzer Yu.L. Seymour M.H. Webber B.R. Catani, S. Longitudinally-invariant k_{\perp} -clustering algorithms for hadron-hadron collisions. *Nuclear Physics B*, 406(1-2):187–224, 1993. cited By (since 1996) 366.
- [37] Yuri L. Dokshitzer et al. Better jet clustering algorithms. *JHEP*, 9708:001, 1997.
- [38] Characterization of Interaction-Point Beam Parameters Using the pp Event-Vertex Distribution Reconstructed in the ATLAS Detector at the LHC. Technical Report ATLAS-CONF-2010-027, CERN, Geneva, May 2010.
- [39] Jet energy scale and its systematic uncertainty in proton-proton collisions at $\sqrt{s}=7$ TeV in ATLAS 2010 data. Technical Report ATLAS-CONF-2011-032, CERN, Geneva, Mar 2011.
- [40] ATLAS Calorimeter Response to Single Isolated Hadrons and Estimation of the Calorimeter Jet Scale Uncertainty. Technical Report ATLAS-CONF-2011-028, CERN, Geneva, Mar 2011.
- [41] E Khramov et al. Study of the Response of the Hadronic Barrel Calorimeter in the ATLAS Combined Test-beam to Pions of Energies from 20 to 350 GeV for Beam Impact Points from 0.2 to 0.65. Technical Report ATL-TILECAL-PUB-2009-007. ATL-COM-TILECAL-2009-006, CERN, Geneva, Apr 2009.

- [42] In-situ pseudorapidity intercalibration for evaluation of jet energy scale uncertainty using dijet events in proton-proton collisions at $\sqrt{s}=7$ TeV. Technical Report ATLAS-CONF-2011-014, CERN, Geneva, Mar 2011.
- [43] Volker Blobel. An Unfolding method for high-energy physics experiments. pages 258–267, 2002.
- [44] Bogdan Malaescu. An Iterative, dynamically stabilized method of data unfolding. 2009.
- [45] Bogdan Malaescu. An Iterative, Dynamically Stabilized(IDS) Method of Data Unfolding. 2011.